Joint 21-cm and CMB Forecasts for Constraining Self-Interacting Massive Neutrinos

Sarah Libanore,[1, *] Subhajit Ghosh,[2, †] Ely D. Kovetz,[1, 2] Kimberly K. Boddy,[2] and Alvise Raccanelli[3, 4, 5]

[1]*Department of Physics, Ben-Gurion University of the Negev, Be'er Sheva 84105, Israel*
[2]*Texas Center for Cosmology and Astroparticle Physics, Weinberg Institute,*
Department of Physics, The University of Texas at Austin, Austin, TX 78712, USA
[3]*Dipartimento di Fisica e Astronomia "Galileo Galilei", Università di Padova, I-35131 Padova, Italy*
[4]*INFN Sezione di Padova, I-35131 Padova, Italy*
[5]*INAF-Osservatorio Astronomico di Padova, Italy*

Self-interacting neutrinos provide an intriguing extension to the Standard Model, motivated by both particle physics and cosmology. Recent cosmological analyses suggest a bimodal posterior for the coupling strength $G_{\rm eff}$, favoring either strong or moderate interactions. These interactions modify the scale-dependence of the growth of cosmic structures, leaving distinct imprints on the matter power spectrum at small scales, $k > 0.1\,{\rm Mpc}^{-1}$. For the first time, we explore how the 21-cm power spectrum from the cosmic dawn and the dark ages can constrain the properties of self-interacting, massive neutrinos. The effects of small-scale suppression and enhancement in the matter power spectrum caused by self-interacting neutrinos propagate to the halo mass function, shaping the abundance of small– and intermediate–mass halos. It is precisely these halos that host the galaxies responsible for driving the evolution of the 21-cm signal during the cosmic dawn. We find that HERA at its design sensitivity can improve upon existing constraints on $G_{\rm eff}$ and be sensitive to small values of the coupling, beyond the reach of current and future CMB experiments. Crucially, we find that the combination of HERA and CMB-S4 can break parameter degeneracies, significantly improving the sensitivity to $G_{\rm eff}$ over either experiment alone. Finally, we investigate the prospects of probing neutrino properties with futuristic Lunar interferometers, accessing the astrophysics-free 21-cm power spectrum during the dark ages. The capability of probing small scales of these instruments will allow us to reach a percent-level constraint on the neutrino self-coupling.

I. INTRODUCTION

Over the past decades, cosmology has made remarkable progress in mapping the large-scale structure (LSS) of the Universe and refining our understanding of fundamental physics. Observations of the cosmic microwave background (CMB) and large-scale galaxy surveys have provided stringent constraints on key cosmological parameters. These cosmological observations are sensitive to the fundamental interaction among particles, thus opening a window to search for physics beyond the Standard Model (SM). Further progress to scrutinize the concordance ΛCDM model and explore alternative cosmological scenarios requires new and complementary datasets.

Among the open questions in cosmology and fundamental physics, the properties of neutrinos remain elusive. In the SM, there are three flavors of massless neutrinos. However, observations of neutrino oscillations indicate at least two of the three flavors have non-zero mass [1–9], but the absolute mass of the neutrino states and possible beyond-SM interactions remain unknown.

Using cosmological observations is a promising route to study the properties of neutrinos, due to the large abundance of neutrinos in the early Universe [10–15]. Neutrinos affect the growth of structure differently at high and low redshifts due to their transition between the relativistic and non-relativistic regimes. The precise redshift when this transition occurs depends on the sum of neutrino masses M_ν, which has been constrained, for example, using *Planck* 2018 CMB data [16] and baryon acoustic oscillations (BAO) results from the Dark Energy Survey Instrument (DESI) [17–20]. Currently, the *Planck* + DESI joint analysis places the strongest constraint on M_ν [20], beating even the design sensitivity of current and upcoming terrestrial experiments [21, 22]. However, current observations are not yet sensitive enough to distinguish between different neutrino mass hierarchies [23].

Cosmological observations are also particularly sensitive to the free-streaming nature of neutrinos. In the SM, neutrinos free-stream after decoupling from the plasma around Big Bang Nucleosynthesis. Preventing neutrinos from free-streaming enhances the CMB power spectra, modifies its acoustic phase-shift, and imprints characteristic features in the matter power spectrum [24–36]. A departure from the free-streaming nature would inevitably point towards the existence of beyond-SM physics in the neutrino sector.

An intriguing possibility is that the SM neutrinos experience self-interactions, which can be modeled by a 4-Fermi effective operator, induced by a mediator of mass $\mathcal{O}({\rm MeV})$ [24]. Recent studies have shown that measurements of the CMB and LSS show a moderate to strong preference for *strong* neutrino self-interactions, almost six orders of magnitude stronger than SM weak interactions [24, 27–29, 31–33, 37–41] Moreover, these strong self-interaction scenarios have the potential to partially relax the Hubble and S_8 tensions [39, 41].

Additionally, small-scale cosmological probes are cru-

arXiv:2504.15348v1 [astro-ph.CO] 21 Apr 2025

cial for studying self-interacting neutrinos across a wide range of interaction strengths. Previous work studied the constraining power of the 21-cm power spectrum on interactions between neutrinos and dark matter [42, 43] and of the 21-cm global signal on self-interactions between ultra-high-energy neutrinos [44]. The effects at small scales may also be correlated with those at large scales, and a global analysis could strengthen constraints and break degeneracies with other cosmological and astrophysical parameters. For example, high-redshift 21-cm data can be used in combination with CMB measurements to reduce the degeneracy between the optical depth τ and M_ν in CMB data, enabling the ability to constrain both parameters with good accuracy [45, 46].

In this paper, we study how the high-redshift 21-cm power spectrum can probe the existence of self-interacting neutrinos. Furthermore, we investigate the interplay between future CMB and 21-cm observations and their ability to place joint constraints on self-interaction coupling strength G_{eff} and the sum of neutrino masses M_ν. We perform forecasts for three different fiducial models with strong (SIν), moderate (MIν), and mild (mIν) neutrino self-interactions. The SIν model is based on the CMB results from Ref. [47], which found a preference for self-interactions over ΛCDM. The MIν and mIν models are ones beyond the reach of current CMB experiments.

Our main focus is the 21-cm power spectrum from the cosmic dawn, which probes small scales indirectly due to the relation between matter fluctuations and the abundance of the first galaxies. We forecast for the design sensitivity of the Hydrogen Epoch of Reionization Array (HERA) [48], which is a precursor of the Square Kilometer Array Observatory (SKAO) [49, 50] and already sets upper limits on the most extreme astrophysical models [51–53]. We also forecast for futuristic observations of the 21-cm signal from the dark ages, which rely on advanced versions of SKAO or proposed Lunar detectors (e.g., Refs. [54–60]). Even if very challenging to access, the 21-cm signal from the dark ages would be extremely informative for cosmology, since it would be free from degeneracies with astrophysical sources, and it could be used to trace fluctuations on small scales that are still in the linear regime. For the CMB, our forecasts use the specifications for the wide survey proposed for CMB-S4.

We find that the design sensitivity of HERA has much stronger constraining power on G_{eff} over CMB-S4 for the MIν and mIν models, since the CMB sensitivity is limited by Silk damping [61]; for the SIν model, CMB-S4 is the more sensitive probe. In all cases, the combination of CMB-S4 and HERA outperforms either experiment alone, permitting 2σ constraints of $\sim 10\%$ on $\log_{10} G_{\text{eff}}$. For the SIν model, including HERA improves upon the CMB-S4 constraint through its more precise determination of τ. For the mIν model, CMB-S4 breaks the degeneracy in the 21-cm power spectrum between M_ν and small G_{eff}, providing a remarkable improvement in the sensitivity to G_{eff} over the individual experiments. We also extend our analysis to two configurations of Lunar detectors, and joint analyses with CMB-S4 achieves 2σ constraints of $\sim 1\%$–5% on $\log_{10} G_{\text{eff}}$.

This paper is structured as follows. In Sec. II we summarize the properties of self-interacting neutrinos and review the effects of both standard and self-interacting neutrinos on the CMB and the matter power spectrum. In Sec. III we introduce the 21-cm power spectrum and discuss its constraining power on the small-scale regime. In Sec. IV we introduce our forecasting formalism, describe our simulation setup, and summarize the properties assumed for the detectors included in our study. In Sec. V we present our results for the CMB, 21-cm cosmic dawn, and 21-cm dark ages, as well as results from joint analyses between the CMB and the 21-cm signal. We conclude in Sec. VI.

Throughout this paper, the effects of neutrino self-interaction on CMB and the matter power spectrum are calculated using nuCLASS[1], which is a modified version of the Boltzmann solver CLASS [62][2], and we have made our code publicly available. The analysis of the 21-cm signal uses simulations produced with 21cmFirstCLASS [63–65][3], which is an extension of the semi-analytical simulation code 21cmFAST v3 [66][4].

II. COSMOLOGICAL EFFECTS OF SELF-INTERACTING NEUTRINOS

Cosmological neutrinos play an important role in the growth of cosmic structures and have a significant impact on cosmological observables (e.g., see Refs. [67–69] for reviews). At very high redshift, neutrinos are relativistic particles that are initially coupled to the photon-baryon fluid through weak interactions. As the Universe expands, these interactions become inefficient, and neutrinos decouple during the radiation-dominated era at $T \sim 1\,\text{MeV}$. After decoupling, neutrinos free stream and have a relativistic energy density $\rho_\nu \simeq [1 + 7/8(4/11)^{4/3}N_{\text{eff}}]\rho_\gamma$ [70, 71], where ρ_γ is the photon energy density and N_{eff} is the effective number of relativistic neutrino-like species. Massive neutrinos eventually become non-relativistic due to the Hubble expansion and contribute instead as a matter component of the Universe. However, they maintain a high thermal velocity that prevents them from clustering on small scales [72].

Incorporating self-interactions alters the standard cosmological impact of neutrinos. The primary effect is the modification of their free-streaming nature: self-interactions drive neutrinos toward more fluid-like behavior. There are well-motivated beyond-SM scenarios in which neutrinos possess self-interactions [73–77], and

---

[1] https://github.com/subhajitghosh-phy/nuCLASS
[2] https://github.com/lesgourg/class_public
[3] https://github.com/jordanflitter/21cmFirstCLASS
[4] https://pypi.org/project/21cmFAST/

	ΛCDM	SIν	MIν	mIν
$\log_{10} G_{\rm eff}$	–	-1.77	-4	-5
h	0.673	0.67	0.673	0.673
Ω_b	0.0493	0.0498	0.0493	0.0493
Ω_c	0.2612	0.2595	0.2612	0.2612
$10^9 A_s$	2.093	1.959	2.093	2.093
n_s	0.9637	0.9298	0.9637	0.9637
$N_{\rm eff}$	3.01	2.82	3.01	3.01
M_ν	0.051	0.08	0.051	0.051
τ (Sec. II and III)	0.052	0.052	0.052	0.052
τ (Sec. IV)	0.052	0.045	0.054	0.053

TABLE I. Fiducial values of the cosmological parameters for ΛCDM and the three models under consideration. These parameters are the neutrino self-interaction coupling strength $G_{\rm eff}$ (in MeV^{-2}), Hubble parameter h, baryon energy density Ω_b, cold dark matter energy density Ω_c, primordial amplitude A_s, primordial spectral tilt n_s, effective number of relativistic neutrino-like species $N_{\rm eff}$, sum of neutrino masses M_ν, and optical depth τ. We use the top set of values for τ when describing the cosmological effects of self-interacting massive neutrinos in Secs. II and III. The bottom set of values are estimates from our `21cmFirstCLASS` simulations, assuming the fiducial II scenario astrophysical model in Table II, and we use these values for our analysis in Sec. IV.

we quantify the low-energy effect on cosmology with the effective operator

$$\mathcal{L} \supset G_{\rm eff}(\bar{\nu}\nu)(\bar{\nu}\nu), \tag{1}$$

where ν is the left-handed neutrino and $G_{\rm eff}$ is a dimensionful coupling constant. This interaction can be modeled as $\mathcal{L} \supset g_{\nu,ij}\varphi\bar{\nu}_i\nu_j$, where φ is a scalar mediator and i and j are flavor indices. For simplicity, we consider flavor-universal interactions and set the coupling $g_{\nu,ij} = g_\nu \delta_{ij}$ to be the same for all flavors with no cross-flavor interactions. In this scenario, the effective coupling constant in Eq. (1) is [24, 28]

$$G_{\rm eff} = \frac{|g_\nu|^2}{m_\varphi^2}, \tag{2}$$

where m_φ is the mediator mass. The neutrino self-interaction rate is $\Gamma \propto aG_{\rm eff}^2 T_\nu^5$, where a is the scale factor and T_ν is the neutrino temperature. This formulation has been extensively adopted in the literature to constrain the self-interaction coupling strength with cosmological observables [24, 27–29, 31–33, 37–41].

Throughout this paper, we consider three fiducial models for massive neutrinos with strong (SIν), moderate (MIν), and mild (mIν) self-interactions. The cosmological parameters we use for ΛCDM and for each self-interaction model are listed in Table I. The SIν model uses the best-fit values from Table V of Ref. [47] for

the analysis of *Planck* 2018 TT+TE+EE data [16] combined with BAO measurements from 6dFGS [78], SDSS MGS [79], and BOSS DR12 [80]. However, note that we use the value of $N_{\rm eff}$ from Ref. [47] to define the degeneracy factor between the neutrino species ($\mathrm{deg_{ncdm}}$ in `nuCLASS`); converting back to $N_{\rm eff}$ produces the values we list in Table I.

For the MIν model, we use a value of $G_{\rm eff}$ that is close to the upper bound from Ref. [47]; for the mIν model, we use a value of $G_{\rm eff}$ that is an order of magnitude smaller and is thus well beyond the reach of *Planck*. Since the MIν and mIν models are poorly constrained from CMB data alone, we fix the other parameters to their best-fit ΛCDM+$N_{\rm eff}$+M_ν values from Ref. [47]. In all cases, we use the 95% confidence level (CL) upper limit on M_ν.

In the remainder of this section, we discuss how self-interacting massive neutrinos affect CMB anisotropies and the matter power spectrum, and we further motivate the choices for our fiducial models. We provide details of the modified Boltzmann equations in Appendix A.

A. Effects on the cosmic microwave background

Standard neutrinos impact the CMB through their gravitational effects. Post neutrino decoupling, the relativistic, free-streaming neutrinos have a larger sound speed than the photon-baryon fluid, so the neutrinos gravitationally pull the photon-baryon fluid as their density perturbation modes oscillate. This effect induces a phase shift of the CMB acoustic peaks towards larger scales (i.e., smaller multipoles ℓ) [35, 81]. Due to the free-streaming effects, neutrinos also diminish metric potentials (as we discuss in Sec. II B) and thus suppress the amplitude of the CMB power spectra C_ℓ at high multipoles. The magnitude of these effects depends on $N_{\rm eff}$ and M_ν.

If neutrinos posses sufficient self-interactions after they decouple (from the photon-baryon fluid), they continue behaving as a fluid until their self-interactions decouple, thus delaying the onset of neutrino free streaming. Only the scales that enter the horizon after self-decoupling experience the same gravitational effect from free-streaming neutrinos that is expected in ΛCDM. Scales that enter the horizon before self-decoupling (and after neutrino decoupling) are not subject to the standard effects of neutrino free streaming; thus, on these scales, neutrino self-interactions induce an enhanced amplitude of CMB acoustic peaks and a shift towards larger multipoles, relative to ΛCDM. The enhancement and shift are degenerate with n_s and the angular size of the acoustic horizon θ_*, respectively [24, 28, 31, 37].

Because of the degeneracy between $G_{\rm eff}$ and n_s, previous CMB+LSS studies of self-interacting neutrinos have found a bimodal posterior for $\log_{10} G_{\rm eff}$ [24, 27–29, 31–33, 37–41], with a tight posterior peak around $\log_{10} G_{\rm eff} \sim [-1.4, -1.8]$, thereby motivating our SIν benchmark model. We note that although we assume
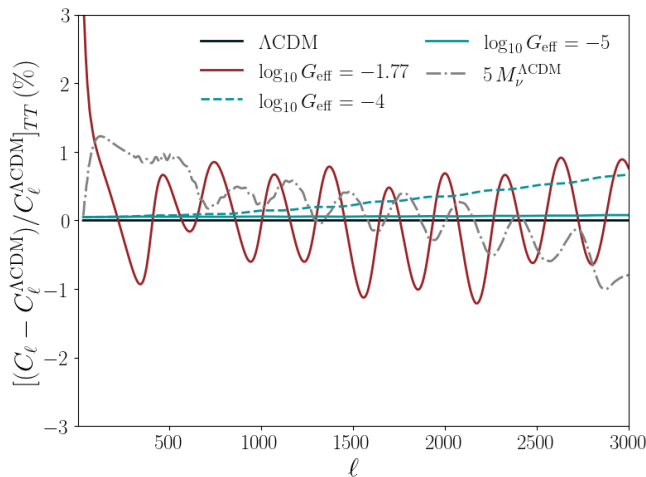
FIG. 1. Residuals of the CMB temperature power spectrum for strong (SIν, solid red), moderate (MIν, dashed cyan), and mild (mIν, solid cyan) neutrino self-interactions with respect to ΛCDM. We use the fiducial values listed in Table I. For comparison, the dot-dashed gray line illustrates the effect of increasing M_ν in ΛCDM.

flavor-universal interactions, there is also a peak in G_{eff} around the same values for flavor-specific interactions [31, 32]. Since the value of θ_* (as well as N_{eff}) shifts for these models, self-interacting neutrinos have been proposed as a possible solution to the Hubble tension [28, 31]; however, subsequent studies [29, 39, 47, 82] have shown that including BAO measurements [78–80] or CMB polarization data in the analysis significantly reduces the viability of resolving the tension.

Figure 1 demonstrates the impact of self-interacting neutrinos on the CMB temperature power spectrum. For SIν, free streaming is delayed up to a time around matter-radiation equality, leading to a net shift in the acoustic peak locations and their amplitudes. In order to maintain a good fit to *Planck*, these changes are partially compensated by changes to A_s, n_s, and τ [47].

Moving away from the SIν regime towards smaller values of G_{eff}, previous studies have simply found upper limits, since the effects of self-interactions are pushed to smaller scales, corresponding to an earlier self-interaction decoupling time. Our MIν model corresponds to a value of G_{eff} near the upper limit in Ref. [47], for which the scales of interest start to become more difficult to probe with the CMB due to Silk damping. We choose a value of G_{eff} for the mIν model that is an order of magnitude below that for the MIν, so detecting the impact of mIν on the CMB would require a future instrument with sensitivity to smaller scales than *Planck*.

In Fig. 1, the phase shift due to delayed free-streaming occurs on scales $\ell > 3000$, which is beyond the accessibility of *Planck*, for the MIν and mIν models. The only visible effect in the figure is the slightly larger amplitude at high multipoles, which does not produce a sufficient deviation from ΛCDM to be detected with *Planck*.

As a point of comparison in Fig. 1, we show the effect of changing M_ν in a cosmology with no neutrino self-interactions, using the ΛCDM fiducial cosmology in Table I, except we fix $\theta_\star$ instead of h to its best-fit *Planck* value and choose a larger sum of neutrino masses, set to five times that of the ΛCDM benchmark ($M_\nu = 5M_\nu^{\Lambda\text{CDM}}$). An increase in the sum of neutrino masses causes a suppression in the temperature power spectrum at high multipoles, while an increase in the neutrino self-interaction strength (from mIν to MIν) causes an enhancement.

B. Effects on the linear matter power spectrum

Massive neutrinos suppress matter clustering at scales that enter the horizon when neutrinos are relativistic. The suppression stems from two physical effects: relativistic neutrinos themselves do not cluster, and their radiation pressure hinders the clustering of cold dark matter and baryons, further suppressing structure formation. Figure 2 shows the additional suppression in the matter power spectrum for $M_\nu = 5M_\nu^{\Lambda\text{CDM}}$.

The free-streaming nature of neutrinos also impacts the linear matter power spectrum $P_m(k, z)$. Free-streaming induces a difference in the evolution of the potentials ϕ and ψ, which drive the growth of matter perturbations [81, 83]:

$$d_c(k,t) = -\frac{9}{2}\phi_P + k^2 \int dt' \, t' \psi(k,t') \ln\left(\frac{t'}{t}\right), \qquad (3)$$

where $d_c = \delta_c - 3\phi$, δ_c is the dark matter density contrast in Newtonian gauge ($d_c = \delta_c$ at late times), ϕ_P is the primordial value of ϕ on large scales, and t is conformal time. In particular, $\psi(k,t)$ decays for modes that enter the horizon during the radiation-dominated era. In the presence of free-streaming neutrinos, the anisotropic stress is $\phi - \psi \neq 0$, which results in a smaller superhorizon initial value of ψ and thus a faster decay [67].

Incorporating neutrino self-interactions suppresses anisotropic stress before the onset of neutrino free streaming. As a result, there is a scale-dependent impact on $P_m(k, z)$, as shown in Fig. 2 for $z = 0$. Small-scale modes that enter the horizon while neutrinos are still tightly self-coupled experience an anisotropic stress $\phi - \psi \sim 0$; therefore, the initial value of ψ is higher, but its decay is slower. The overall effect is the suppressed growth of d_c, relative to ΛCDM. Neutrinos also affect the scale dependence of the galaxy bias (see e.g., [84]), which we do not include in this work. In contrast, modes that enter the horizon close to neutrino self-decoupling experience a boost in the initial value of ψ, while subsequent evolution returns it to its ΛCDM behavior. Thus, the amplitude of density perturbations for these modes is strongly boosted. Finally, large-scale modes that enter the horizon after the neutrinos have self-decoupled and are free streaming remain unchanged with respect to ΛCDM.
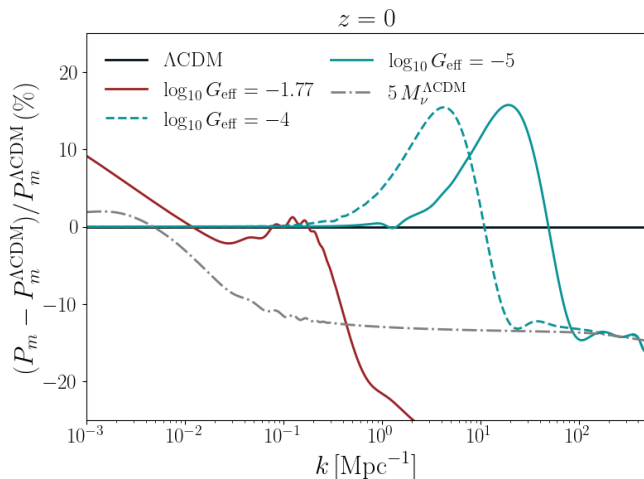
FIG. 2. Residuals of the linear matter power spectrum at $z = 0$. The legend is the same as in Fig. 1.

Figure 2 highlights the impact of neutrino interactions on the matter power spectrum, with respect to ΛCDM. The scale that enters the horizon around neutrino self-decoupling experiences the largest boost in $P_m(k)$. For the MIν and mIν models, the boost occurs on scales $k \sim 1 - 100\,\mathrm{Mpc}^{-1}$, and there is a moderate $\sim 10\%$ suppression at larger k. For the SIν model, the shape of $P_m(k)$ with respect to ΛCDM arises from two effects. First, there is a boost $k \sim 0.1\,\mathrm{Mpc}^{-1}$ caused by the neutrino self-interactions. Second, the primordial spectral tilt for the SIν model is smaller than the tilt for ΛCDM, as listed in Table I. The smaller tilt results in the relative enhancement of $P_m(k)$ on very large scales, as well as the steep suppression for $k \gtrsim 1\,\mathrm{Mpc}^{-1}$.

The scale-dependent nature of the deviation from ΛCDM in all models is crucial for probing them using small-scale observations. The large-k suppression is similar in magnitude to the suppression from additional neutrino mass, which is controlled by the value M_ν. However, the notable enhancement of the matter power spectrum for the moderate and mild self-interaction models provides a distinct feature that can help distinguish these models.

III. IMPACT OF SELF-INTERACTING NEUTRINOS ON THE 21-CM SIGNAL

At redshift $z \gtrsim 6$, the 21-cm line is sourced by neutral hydrogen (H) in the intergalactic medium (IGM). To study its signal, the main observable quantities are the brightness temperature

$$T_{21}(z) = \frac{T_s(z) - T_{\mathrm{CMB}}(z)}{1+z} e^{-\tau_{21}(z)}, \qquad (4)$$

and its spatial fluctuations δT_{21}, which are used to construct the 21-cm power spectrum

$$\Delta^2_{21}(k, z) = \frac{k^3}{2\pi^2} \delta^D(\boldsymbol{k} - \boldsymbol{k}') \langle \delta T_{21}(\boldsymbol{k}, z) \delta T^*_{21}(\boldsymbol{k}', z) \rangle. \quad (5)$$

The evolution of $T_{21}(z)$ in Eq. (4) follows the evolution of the difference between the CMB temperature T_{CMB} and the spin temperature $T_s(z)$, which provides an estimate of the relative number densities of H in the triplet and singlet states. In turn, the evolution of $T_s(z)$ is driven by the coexistence of different processes that excite H in the IGM, coupling its value either with the CMB temperature or with the gas temperature $T_{\mathrm{gas}}(z)$. The 21-cm optical depth is [85]

$$\tau_{21} = (1 + \delta_m) x_{\mathrm{HI}} \frac{T_0}{T_s} \frac{H(z)}{\partial v_r} (1 + z), \qquad (6)$$

where T_0 is a normalization factor, x_{HI} is the neutral hydrogen fraction, δ_m is the matter density contrast, $H(z)$ the Hubble parameter, and ∂v_r the line-of-sight gradient of the velocity. We summarize the key expressions required to model the evolution of all these quantities in Appendix B.

Based on the dominant coupling process, we can distinguish between two different eras:

- the dark ages ($z \sim [30, 200]$), during which T_{gas} cools adiabatically and T_s is coupled to its value via collisional coupling between the H atoms; and

- cosmic dawn ($z \sim [6, 30]$), during which radiation sourced by stars and galaxies couples T_s to T_{gas}, while at the same time heating the gas and increasing T_{gas}. The cosmic dawn is followed by the epoch of reionization ($z \sim [4, 6]$), in which UV radiation from astrophysical sources ionizes the gas, thus decreasing the H optical depth τ_{21} and damping the 21-cm signal until it disappears.

The amplitude of the 21-cm signal is strongly affected by the choice of the underlying cosmological and astrophysical models. Extensive reviews can be found in Refs. [85–87] and references therein; we simply visualize the evolution of the average value of $T_{21}(z)$, namely the global signal, in Fig. 3. We obtain these various $T_{21}(z)$ curves by running `21cmFirstCLASS` under different choices of cosmological and astrophysical parameters, evolving the 21-cm signal consistently from recombination to reionization.

Figure 3 highlights how different neutrino properties can speed up or slow down the evolution of the global 21-cm signal during cosmic dawn. However, it also shows how such changes can be degenerate with the choice of astrophysical parameters, such as the star formation efficiency $f_{*,10}$, which we discuss in Sec. III A 2. Since different neutrino properties introduce scale-dependent effects in the matter power spectrum, we expect to be able to break degeneracies with the astrophysical parameters by
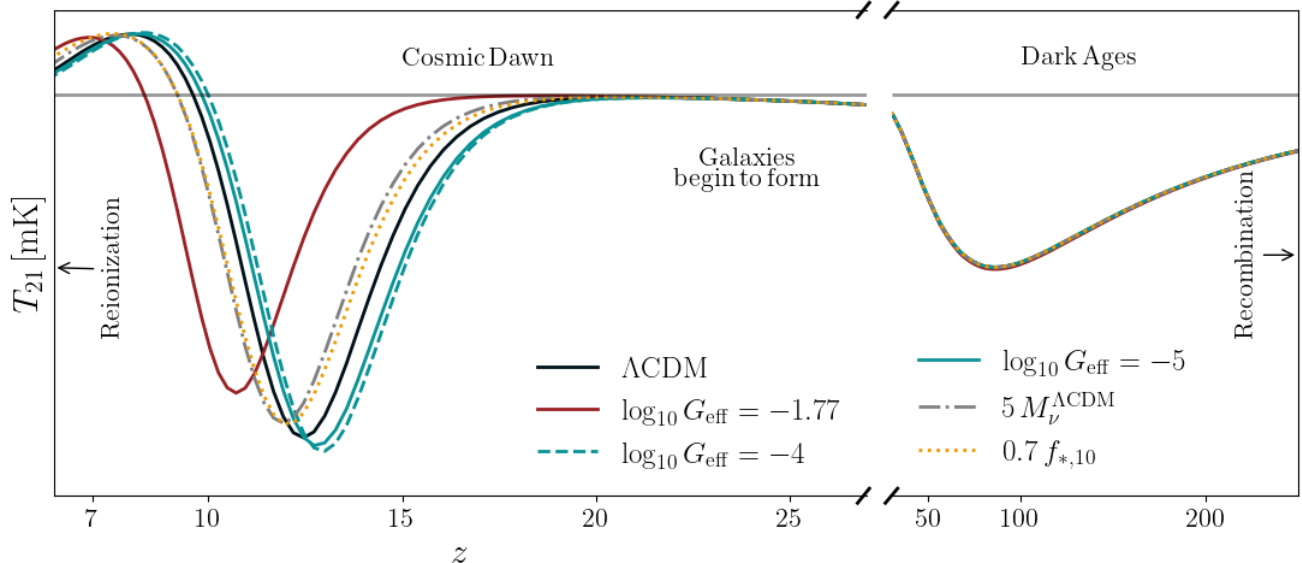
FIG. 3. Illustrative plot of the 21-cm global signal across cosmic history. The evolution of $T_{21}(z)$ is estimated from the `21cmFirstCLASS` simulation, which evolves the 21-cm signal consistently with the chosen cosmological and astrophysical models, from recombination ($z \sim 1100$) down to reionization ($z \sim 6$). The legend is the same as in Fig. 1, but we also show the effect of reducing the star formation efficiency $f_{*,10}$ from its baseline. The horizontal line shows $T_{21}(z) = T_{\mathrm{CMB}}$.

looking at the 21-cm power spectrum $\Delta_{21}^2(k, z)$ instead. Using $\Delta_{21}^2(k, z)$ is also crucial to detect signatures of neutrino properties during the dark ages; here, in fact, the global signal is blind to such models, since they do not introduce extra energy injection in the IGM compared to ΛCDM.

In the following, we recap the key aspects required to understand how the amplitude of the 21-cm signal evolves and how $\Delta_{21}^2(k, z)$ traces the shape of the underlying $P_m(k, z)$, highlighting why we expect it to be sensitive to the small scales affected by the self-interacting neutrino models.

A. Cosmic dawn

When the first galaxies in the Universe begin to form, their radiation has enormous consequences for the conditions of the IGM, as it alters the status of the atoms in the gas, increases the gas temperature, and ionizes neutral H. The coupling between T_s and T_{gas} during this epoch is caused by the Lyman-α (Lyα) flux emitted by the stars, which is easily absorbed by H through the Wouthuysen-Field effect [88, 89]. At the same time, the X-ray component of the radiation heats the gas [90–92], and the ability of the UV component to escape into the IGM turns on the epoch of reionization [66, 93].

As we describe in Secs. III A 2 and III A 1, the detailed evolution of $T_{21}(z)$ and its fluctuations during cosmic dawn depends both on the shape of the underlying matter power spectrum and on the model of star formation. Therefore, the choice of cosmology and astrophysics impacts the shape of the expected 21-cm power spectrum during the cosmic dawn. As an example, in Fig. 4, we show the $\Delta_{21}^2(k, z)$ produced by our `21cmFirstCLASS` simulations. We compare the neutrino self-interaction models with ΛCDM at fixed z and at fixed k, highlighting the features that each neutrino model introduces, which may be distinguishable with the sensitivity of upcoming 21-cm detectors. Moreover, the figure demonstrates that by using $\Delta_{21}^2(k, z)$, we can break degeneracies between astrophysical and cosmological parameters, due to the scale-dependent effect from cosmology.

1. Halo mass function

The key ingredient to model the evolution of $\Delta_{21}^2(k, z)$ is the star formation rate density (SFRD) $\dot{\rho}_*(\boldsymbol{x}, z)$. This determines the intensity of the Lyα radiation that couples T_s to T_k, as well as the intensity of the X-ray heating. A summary of the key quantities required to model these processes can be found in Appendix B. Following Refs. [94, 95], we model the SFRD as a function of the star formation rate (SFR) $\dot{M}_*$, which depends on the host dark matter halo mass M_h, convolved with the local halo mass function (HMF) $dn/dM_h(\boldsymbol{x}, z)$:

$$\dot{\rho}_*(\boldsymbol{x}, z) = \int_{M_{\mathrm{min}}}^{\infty} dM_h \frac{dn}{dM_h}(\boldsymbol{x}, z) \dot{M}_*(M_h, z) f_{\mathrm{duty}}(M_h),$$

(7)

where $f_{\mathrm{duty}}(M_h)$ is the duty cycle, which suppresses the SFR below a certain turnover mass, M_{turn}. We set $M_{\mathrm{min}} = 10^5 \, M_{\odot}$, but this choice does not affect the final result, as long as $M_{\mathrm{min}} < M_{\mathrm{turn}}$.

We can rewrite Eq. (7) in terms of the local collapse
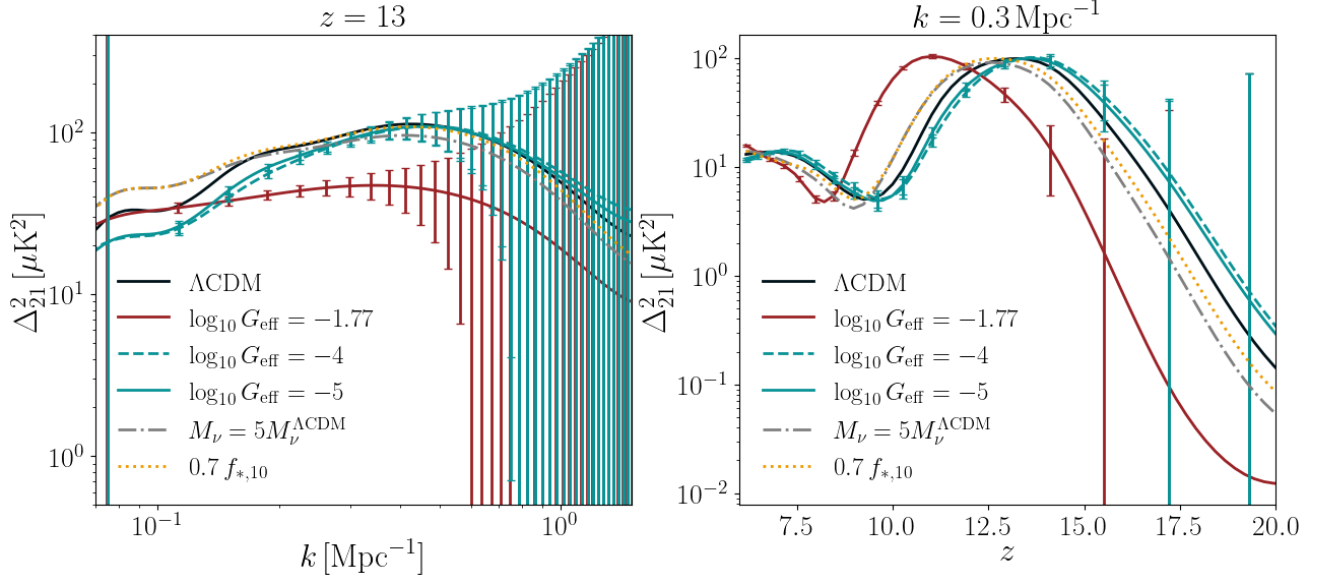
FIG. 4. 21-cm power spectrum during cosmic dawn for fixed z (left) and for fixed k (right). The legend is the same as in Fig. 1. We show $z = 13$, which coincides with the redshift of the 21-cm absorption peaks in Fig. 3. We also show $k = 0.3 \, \mathrm{Mpc}^{-1}$, since it is in the range of scales already probed by HERA Phase I [51–53]. The errorbars represent the design sensitivity of the HERA detector we adopt for our analysis in Sec. IV A.

fraction of matter into halos with mass $M_h \geq M_{\min}$

$$f_{\mathrm{coll}}(\boldsymbol{x}, z, M_{\min}) = \frac{1}{\bar{\rho}_{m,0}} \int_{M_{\min}}^{\infty} dM_h \frac{dn}{dM_h}(\boldsymbol{x}, z) M_h, \quad (8)$$

where $\bar{\rho}_{m,0}$ is the mean matter density at $z = 0$. As we discuss in detail in Sec. III A 2, the star formation rate can be approximated as a power law of the host halo mass, $\dot{M}_*(M_h) = A_{\mathrm{SFR}} M_h^{\alpha_*}/\bar{\rho}_m$, where the A_{SFR} factor is independent of M_h, and α_* depends on the model. Since

$$\frac{df_{\mathrm{coll}}}{dM_h}(\boldsymbol{x}, z) = -\frac{M_h}{\bar{\rho}_m} \frac{dn}{dM_h}, \quad (9)$$

we can define

$$\mathcal{F}_{\mathrm{coll}}(\boldsymbol{x}, z) = -\int d\log M_h \frac{df_{\mathrm{coll}}}{dM_h}(\boldsymbol{x}, z) M_h^{\alpha_*} f_{\mathrm{duty}}(M_h), \quad (10)$$

so that the SFRD can be re-expressed as

$$\dot{\rho}_*(\boldsymbol{x}, z) = A_{\mathrm{SFR}} \mathcal{F}_{\mathrm{coll}}(\boldsymbol{x}, z). \quad (11)$$

This form is particularly helpful in the context of simulations, since it allows us to relate the local SFRD to the local density field. According to the extended Press-Schechter (EPS) formalism [96, 97], the collapsed fraction in Eq. (8) can also be estimated based on the local density field smoothed over comoving scale $R = [3M_h/(4\pi\bar{\rho}_{m,0})]^{-3}$, which we denote as $\delta_{m,R}$. We have

$$f_{\mathrm{coll},R}^{\mathrm{EPS}}(\boldsymbol{x}, z, M_{\min}) = \mathrm{erfc}\left[\frac{\delta_c - \delta_{m,R}(\boldsymbol{x}, z)}{\sqrt{\sigma^2(M_{\min}, z) - \sigma^2(M_h, z)}}\right], \quad (12)$$

where $\delta_c = 1.686$ is the critical density for collapse, and the smoothed variance of the matter field is

$$\sigma^2(M_h, z) = \int_0^{\infty} \frac{dk}{k} P_m(k, z) W_R^2(k), \quad (13)$$

and we use a real-space spherical top-hat window function $W_R(k) = 3[\sin(kR) - (kR)\cos(kR)]/(kR)^3$.

In the original EPS formulation, the smoothed overdensity $\delta_{m,R}(\boldsymbol{x}, z)$ is linearly evolved; we do the same in our `21cmFirstCLASS` simulation. However, we note that using a non-linear evolution through 2nd-order Lagrangian perturbation theory [98, 99] would be justified, since it seems to provide better agreement with radiative transfer simulations in the epoch of reionization [65].

Combining Eqs. (8), (10), and (12), we can estimate $\mathcal{F}_{\mathrm{coll}}^{\mathrm{EPS}}(\boldsymbol{x}, z)$ and, if needed, scale this factor to any other HMF formalism through [66, 100, 101]

$$\mathcal{F}_{\mathrm{coll}}(\boldsymbol{x}, z) = \mathcal{F}_{\mathrm{coll}}(z) \frac{\mathcal{F}_{\mathrm{coll}}^{\mathrm{EPS}}(\boldsymbol{x}, z)}{\langle \mathcal{F}_{\mathrm{coll}}^{\mathrm{EPS}}(\boldsymbol{x}, z)\rangle_{\boldsymbol{x}}}, \quad (14)$$

where $\langle \mathcal{F}_{\mathrm{coll}}^{\mathrm{EPS}}(\boldsymbol{x}, z)\rangle_{\boldsymbol{x}}$ is the spatial mean in the EPS case and $\mathcal{F}_{\mathrm{coll}}(z) \propto \int dM_h d\bar{n}/dM_h(z) M_h$ is proportional to the mean HMF. For our analysis in Sec. IV, we rely on the Sheth, Mo, and Tormen HMF [102–104]

$$\frac{d\bar{n}}{dM_h}(z) = -\frac{\Omega_m \rho_c}{M_h} \frac{d\log \sigma}{dM_h} \sqrt{2\pi} A_{\mathrm{ST}} (1 + \hat{\nu}^{-2p_{\mathrm{ST}}}) \hat{\nu} e^{-\hat{\nu}^2/2}, \quad (15)$$

where $\rho_c = 3H_0^2/(8\pi G)$ is the critical density, $A_{\mathrm{ST}} = 0.353$, $p_{\mathrm{ST}} = 0.175$, and $\hat{\nu} = \sqrt{0.73}\,\delta_c/\sigma$.

The spatial fluctuations in T_{21} during cosmic dawn are mainly driven by inhomogeneities in the distribution of
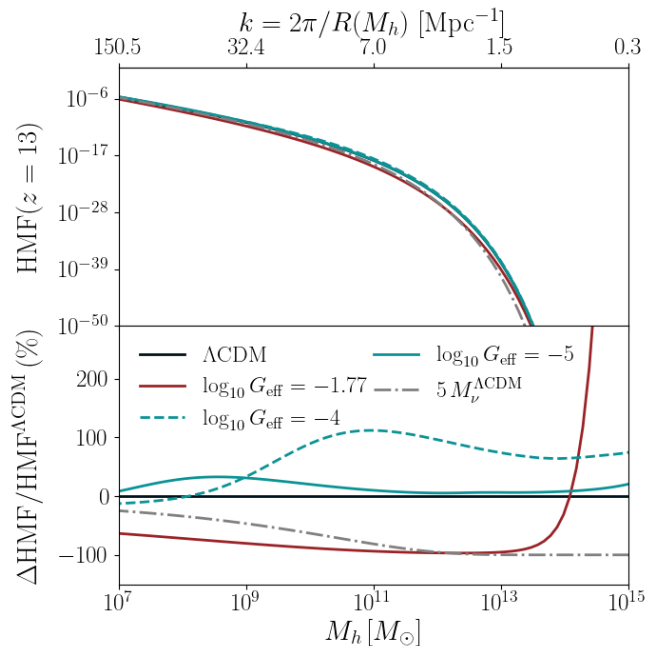
FIG. 5. Halo mass function (top) and its residual with respect to ΛCDM (bottom). The legend is the same as in Fig. 1. Compared with Fig. 2, the effect each model has on the linear matter power spectrum at different scales propagates to variations in the abundance of halos with different M_h.

dark matter halos, where the astrophysical sources form.[5] Therefore, $\Delta^2_{21}(k, z)$ is inevitably related to the HMF and hence to the underlying $P_m(k, z)$. Therefore, any deviation from ΛCDM, such as the ones caused by self-interacting neutrinos, should propagate to the 21-cm signal via the HMF.

In Fig. 5, we compare the HMF at cosmic dawn for ΛCDM with the HMF for the neutrino models of interest for our work. The window function $W_R(k)$ in Eq. (13) provides a k-dependent weight that also depends on $R(M_h)$, so variations of $P_m(k, z)$ over certain k regions roughly translate to variations of the HMF over certain halo masses M_h. Due to the different values of n_s between the SIν model and the fiducial ΛCDM model (see Table I), the HMF is suppressed for halo masses $M_h \lesssim 10^{14} M_\odot$. The small boost of $P_m(k, z)$ at $k \sim 0.1\,\mathrm{Mpc}^{-1}$ in Fig. 2 increases the abundance of halos with $M_h \gtrsim 10^{14} M_\odot$, which are very rare at high z; the 21-cm signal is almost blind to this high-mass end.

In contrast, the shape of $P_m(k, z)$ for the MIν model implies that the number of mini-halos ($M_h \lesssim 10^8 M_\odot$) is suppressed, while the number of halos with $M_h \gtrsim 10^9 M_\odot$ is enhanced. This result is particularly interesting for

[5] Reference [105] recently showed that stochasticity in the astrophysical model has a non-negligible effect on the galaxy luminosity function at cosmic dawn. We expect $\Delta^2_{21}(k, z)$ to be similarly affected [106].

21-cm at cosmic dawn, since galaxies in these halos drive the evolution of H in the IGM. For the mIν model, the smaller value of G_{eff} diminishes these features and shifts them to smaller masses, such that only halos of mass $M_h \in [10^8, 10^{10}] M_\odot$ experience boost in the HMF.

Finally, analogous to our discussion of $P_m(k, z)$ in Sec. II B, increasing M_ν has the opposite effect from the mIν and MIν models over a certain range of scales. Additional neutrino mass suppresses the HMF for all masses above a certain threshold. It is only at very small scales that the increased-M_ν, mIν, and MIν models all suppress the matter power spectrum, which translates into the suppression of very low-mass halos in Fig. 5.

We now discuss the interpretation of the cosmic dawn signals $T_{21}(z)$ and $\Delta^2_{21}(k, z)$ in Figs. 3 and 4, respectively, in light of our HMF results. The change induced in the HMF by self-interacting neutrinos implies that the number of astrophysical sources is also varied, thus advancing or delaying the onset of cosmic dawn.

For example, the increased-M_ν and mIν models shift $T_{21}(z)$ in different directions. More massive neutrinos suppress small scales, reducing the abundance of halos in the small-to-intermediate mass range. Therefore, it takes more time to heat up the gas, and the difference between T_s and the CMB temperature remains large down to a lower redshift, explaining why $T_{21}(z)$ and the amplitude of $\Delta^2_{21}(k, z)$ [shown at $z = 13$ in Fig. 4] are larger as compared to ΛCDM. Note that the SIν model suppresses the abundance of small-to-intermediate mass halos even more than the increased-M_ν model, further delaying cosmic dawn. The mIν model presents the exact opposite effect through its enhancement of power on scales relevant for the 21-cm signal, thereby advancing cosmic dawn.

It is important to note that the features in the matter power spectrum in Fig. 2 propagate to features in the 21-cm power spectrum in Fig. 4 but at different values of k. Small-scale deviations of the matter power spectrum appear at slightly larger scales in the HMF, which correspond to halos that host galaxies whose radiation fields impact the IGM and thus the 21-cm power spectrum at still larger scales. Despite the complications it introduces in the modeling, the SFR is the key to move the indirect effects of the self-interacting neutrino models—and of small-scale physics in general—into regimes that can be actually probed by 21-cm and would be otherwise inaccessible by more direct observations of small-scale structure.

2. Astrophysical model

Finally, to compute the 21-cm signal at cosmic dawn, we need to model the SFR $\dot{M}_*(M_h, z)$ of the first galaxies. The SFR is then used to calculate the radiation fields that drive the evolution of T_s through the SFRD in Eq. (7).

We distinguish between *atomic cooling galaxies* (ACGs) and *molecular cooling galaxies* (MCGs). ACGs are produced inside halos with typical masses $M_h \simeq [10^9, 10^{11}] M_\odot$, while MCGs are associated with mini-

popII		popIII	
$\log_{10} f_{*,10}$	-1.25	$\log_{10} f_{*,7}$	-2.5
$\alpha_{*,10}$	0.5	$\alpha_{*,7}$	0
$\log_{10} f_{\mathrm{esc},10}$	1.35	$\log_{10} f_{\mathrm{esc},7}$	-1.35
$\alpha_{\mathrm{esc},10}$	-0.3	$\alpha_{\mathrm{esc},7}$	-0.3
$\log_{10}(L_{X,10}/\mathrm{SFR})$	40.5	$\log_{10}(L_{X,7}/\mathrm{SFR})$	40.5

TABLE II. Fiducial values of the astrophysical parameters adopted in the `21cmFirstCLASS` simulations for our analysis. For each type of source (popII or popIII stars), we provide the star formation efficiency f_* and corresponding power-law index α_*, the escape fraction f_{esc} and corresponding power-law index α_{esc}, and the soft-band X-ray luminosity per unit star formation rate $L_{X,(10,7)}/\mathrm{SFR}$. All quantities have a 10 or 7 subscript to denote the pivot masses $M_p^{\mathrm{II}} = 10^{10} M_\odot$ and $M_p^{\mathrm{III}} = 10^7 M_\odot$ for the popII and popIII stars, respectively.

halos and thus form at higher z. Inside ACGs and MCGs, star formation is driven by different cooling mechanisms, and they can be roughly associated with population II (popII) and population III (popIII) stars, respectively [107–110].

Based on Refs. [94, 95], we approximate the average SFR for each population as the stellar mass produced over a typical timescale:

$$
\begin{aligned}
\dot{M}_*^{\mathrm{II,III}} &= \frac{M_*^{\mathrm{II,III}}}{0.5 H^{-1}(z)} \\
&= \frac{f_*^{\mathrm{II,III}} M_h \Omega_b/\Omega_c \left(M_h/M_p^{\mathrm{II,III}}\right)^{\alpha_*^{\mathrm{II,III}}}}{0.5 H^{-1}(z)}.
\end{aligned}
\tag{16}
$$

Here, we have assumed that the stellar mass can be simply estimated by scaling the baryon mass inside a halo, $M_h \Omega_b/\Omega_c$, by a mass-dependent efficiency factor, $f_*^{\mathrm{II,III}} \left(M_h/M_p^{\mathrm{II,III}}\right)^{\alpha_*^{\mathrm{II,III}}}$. This is a common approximation in the context of 21-cm simulations; see, e.g., Refs. [111–113] for alternatives.

The pivot masses are $M_p^{\mathrm{II}} = 10^{10} M_\odot$ and $M_p^{\mathrm{III}} = 10^7 M_\odot$; the values of $f_*^{\mathrm{II,III}}$ and $\alpha_*^{\mathrm{II,III}}$ are different for ACGs and MCGs and are summarized in Table II. The difference between popII and popIII stars also determines a different turnover mass $M_{\mathrm{turn}}^{\mathrm{II,III}}$ below which star formation becomes inefficient. This mass enters the calculation of the duty cycle $f_{\mathrm{duty}}(M_h)$ in Eq. (7), which is computed differently in the two scenarios:

$$
f_{\mathrm{duty}}^{\mathrm{II}}(M_h) = \exp\left(-\frac{M_{\mathrm{turn}}^{\mathrm{II}}}{M_h}\right),
\tag{17}
$$

$$
f_{\mathrm{duty}}^{\mathrm{III}}(M_h) = \exp\left(-\frac{M_h}{M_{\mathrm{turn}}^{\mathrm{III}}}\right)\exp\left(-\frac{M_{\mathrm{atom}}}{M_h}\right).
\tag{18}
$$

These two expressions allow for a smooth transition of $f_{\mathrm{duty}}(M_h)$ between the halo-mass regime related to MCGs and the one in which ACGs dominate. The transition occurs at $M_{\mathrm{atom}} = 3.3 \times 10^7 M_\odot [(1+z)/21]^{-3/2}$ [95].
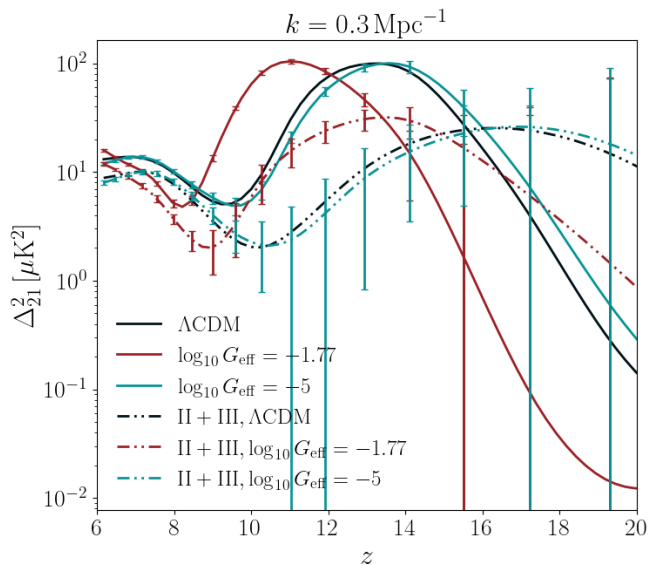
FIG. 6. 21-cm power spectrum during cosmic dawn for fixed k and varying z. The color legend is the same as in Fig. 1. Solid lines represent our baseline (only popII stars), while the dashed lines include the contribution of popIII stars. The errorbars represent the sensitivity of the HERA detector we adopt in our analysis in Sec. IV A.

As for the turnover mass, in the case of ACG galaxies, its value is determined by stellar feedback, such as photoheating and supernovae [114–118]; for MCGs, it is necessary to account for photons in the Lyman-Werner band (11.2–13.6 eV) [107–110, 119] and the suppression due to the relative velocity between dark matter and baryons [120–124] (see, e.g., Ref. [95] for more details and for the full derivation of $M_{\mathrm{turn}}^{\mathrm{II,III}}$).

The last piece of information needed for the astrophysical model is represented by the escape fraction of ionizing photons from galaxies into the IGM, $f_{\mathrm{esc}}^{\mathrm{II,III}}(M_h)$. Following previous literature [94], we parameterize it to be constant in redshift and a function of M_h:

$$
f_{\mathrm{esc}}^{\mathrm{II,III}}(M_h) = f_{\mathrm{esc},M_p^{\mathrm{II,III}}}^{\mathrm{II,III}} \left(\frac{M_h}{M_p^{\mathrm{II,III}}}\right)^{\alpha_{\mathrm{esc}}^{\mathrm{II,III}}}.
\tag{19}
$$

Table II collects the fiducial values of the astrophysical parameters, based on standard choices in the literature (see, e.g., Refs. [94, 95]).

Varying the astrophysical parameters affects, in a scale-independent way, the speed at which cosmic dawn proceeds, hence varying the position and depth of the trough in $T_{21}(z)$ in Fig. 3. Similarly for $\Delta_{21}^2(k,z)$, the peaks rise at different z with different heights in Fig. 4. As a further example, in Fig. 6, we show $\Delta_{21}^2(k,z)$ for ΛCDM and for the SIν and mIν models, under a popII-only and a popII+popIII scenario. As expected, popIII stars anticipate the onset of cosmic dawn and the epoch of reionization; therefore, the peaks of $\Delta_{21}^2(k,z)$ are lower and shifted to higher z.
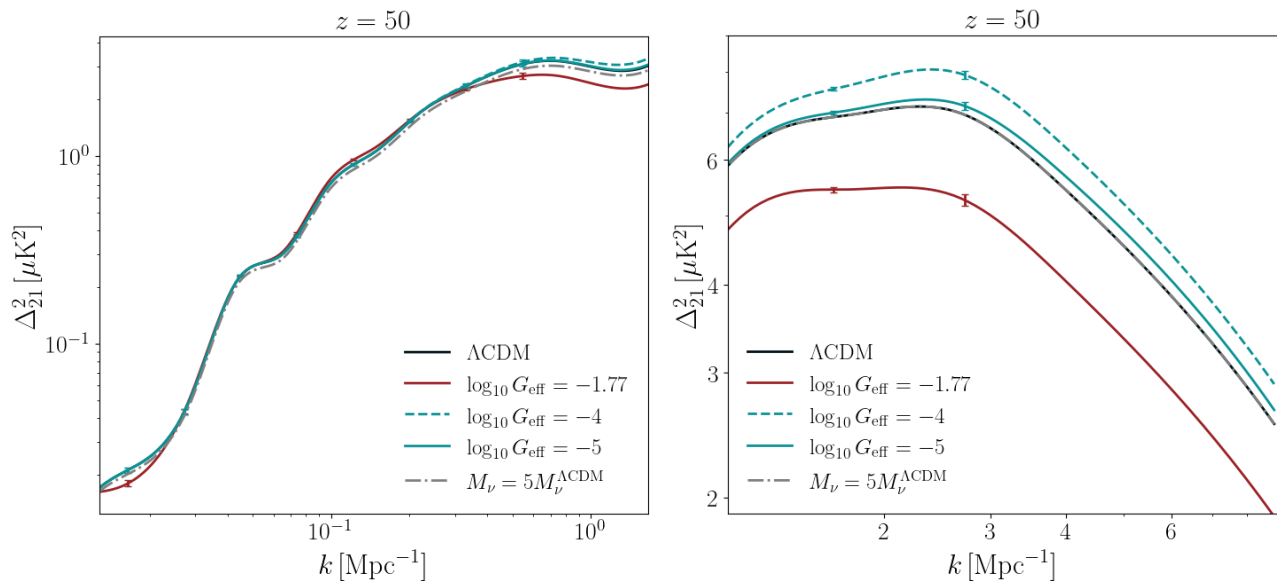
FIG. 7. 21-cm power spectrum during the dark ages for fixed z and varying k. The legend is the same as in Fig. 1. The power spectrum for $k \lesssim 1\,\mathrm{Mpc}^{-1}$ (left) is extracted from the same simulation we generated for cosmic dawn. The power spectrum on smaller scales (right) is extracted from an additional `21cmFirstCLASS` simulation with a smaller box size and higher resolution; see Sec. V. The errorbars show the sensitivity of the Lunar D (left) and LRA1 (right) detectors. The smallest k is set by the size of the simulation box, and the largest by the detector resolution; their position depends on $\Delta \ln(k)$. Details in Sec. IV A.

B.   Dark ages

After recombination and before the formation of the first stars, the Universe is still sufficiently small that H collisional excitations are efficient: T_s couples with $T_{\rm gas}$, and the 21-cm signal can be observed in absorption. The amplitude reaches its largest value around $z \sim 80$, but as the Universe continues expanding, the coupling efficiency and thus the amplitude of T_{21} decrease until cosmic dawn begins.

The fluctuations δT_{21} required to estimate the 21-cm power spectrum during the dark ages are given by [125]

$$\delta T_{21}(\boldsymbol{x}, z) = \frac{T_{21}(z)\delta_v + c_b(z)\delta_b + c_T(z)\delta_{T_k}}{T_{21}(z)}$$
$$\simeq \frac{dT_{21}}{d\delta_b}\delta_b(\boldsymbol{x}, z) + T_{21}(z)\delta_v(\boldsymbol{x}, z) \quad (20)$$

where $\delta_b(\boldsymbol{x}, z)$ is the baryon density contrast, $\delta_v(\boldsymbol{x}, z) = -(1+z)\partial_r v/H(z)$ is the peculiar velocity fluctuation, and $\delta_{T_k}(\boldsymbol{x}, z)$ is the spatial fluctuation of the gas kinetic temperature. In the second line, we neglect the fluctuations in the gas temperature.

Before recombination, baryons are coupled with CMB photons and therefore oscillate without collapsing; after they decouple, baryons begin to follow the dark matter distribution and can be treated as a biased tracer of the underlying dark matter field. However, it is important to account for some subtleties.

First, during dark ages, the coupling between baryons and dark matter is not yet complete, and the evolution

of $\delta_b(\boldsymbol{k}, z)$ must be estimated using the scale-dependent growth factor $\mathcal{D}_b(k, z) = \mathcal{T}_b(k, z)/\mathcal{T}_b(k, z = 0)$, where $\mathcal{T}_b(k, z)$ is the baryon transfer function. Using this growth factor has a non-negligible impact on the computation of $\Delta_{21}^2(k, z)$, compared to the case in which the signal is computed using the total matter fluctuation $\delta_m(k, z)$ or under the approximation of a scale-independent growth factor, $\delta_m(k, z) = \delta_0(k)D(z)$ [63, 65].

Moreover, the relative velocity between baryons and dark matter suppresses small-scale power in $P_m(k, z)$ [120–126]. This suppression propagates to all scales in $\Delta_{21}^2(k, z)$, due to the non-linear relation between δT_{21} and δ_b and due to a large-scale modulation that velocities induce on δ_b.

The 21-cm power spectrum during the dark ages can be theoretically estimated by solving the Boltzmann equations. Its shape fully depends on the underlying cosmological model, particularly on the form of $P_m(k, z)$. However, for consistency, we extract $\Delta_{21}^2(k, z)$ from the same `21cmFirstClass` runs realized for the cosmic dawn.

As an example, Fig. 7 shows $\Delta_{21}^2(k, z)$ at $z = 50$ for ΛCDM and the neutrino models of interest. Note that the deviations of $\Delta_{21}^2(k, z)$ induced by the neutrino models on the dark ages signal occur on scales k more comparable (as compared to the cosmic dawn signal) to those in $P_m(k, z)$. As shown in Fig. 3, the self-interacting neutrino models do not affect $T_{21}(z)$ during the dark ages, since there is no mechanism to impact the evolution of the gas temperature. Variations on $\Delta_{21}^2(k, z)$ are directly sourced by the shape of $P_m(k, z)$ shown in Fig. 2: the SIν

power suppression is due to the smaller value of n_s relative to ΛCDM, while the enhancements for MIν and mIν reflect the bumps in their corresponding $P_m(k, z)$.

To better capture the effects of MIν and mIν in the dark ages, we run a higher-resolution simulation, as discussed in Sec. IV. The resulting 21-cm power spectrum is shown in the right panel of Fig. 7. Features in the Mν and mIν models are in principle distinguishable from ΛCDM for $k \gtrsim 1\,\mathrm{Mpc}^{-1}$, but detecting these scales would require detectors with very high angular resolution.

IV. RUNNING FORECASTS

To simulate the 21-cm signal during both the dark ages and cosmic dawn, we use `21cmFirstCLASS`. The simulation allows us to account for different initial cosmologies, for the effects of the baryon-dark matter relative velocity (suppression of the matter power spectrum and of the minimum halo mass required to form stars [120–126]), for the scale-dependent growth factor and for the evolution of baryon- and dark-matter perturbations.

We choose a box size of $L = 600\,\mathrm{Mpc}$ and a resolution $N_{\mathrm{cell}} = 256$, which provides a k-space resolution between $k_{\mathrm{min}} = 2\pi/L_{\mathrm{box}} \simeq 0.01\,\mathrm{Mpc}^{-1}$ and $k_{\mathrm{max}} = 2\pi N_{\mathrm{cell}}/L_{\mathrm{box}} \simeq 2.5\,\mathrm{Mpc}^{-1}$. This setup allows us to simulate the signal in the sensitivity band with sample variance smaller than the detector noise (see Sec. IV A).

We run a second simulation with $L = 50\,\mathrm{Mpc}$ and $N_{\mathrm{cell}} = 128$ to improve the resolution for our dark ages analysis, accessing scales $0.15\,\mathrm{Mpc}^{-1} \lesssim k \lesssim 10\,\mathrm{Mpc}^{-1}$.

The initial conditions for the simulation are generated by our `nuCLASS` code, which incorporates the effects of neutrino self-interactions. The transfer function and growth factor produced by `nuCLASS` are used in `21cmFirstCLASS` to evolve the simulation consistently with the input cosmology. Since self-interacting neutrinos do not interact with dark matter and baryons, the Boltzmann equations inside the simulation are unaffected. Within `nuCLASS`, we consider three degenerate neutrino species and describe their properties in terms of the coupling strength G_{eff}, the sum of their masses M_ν, and the effective number of relativistic neutrino-like species N_{eff}.

1. Fiducial setup

The fiducial cosmological parameters we use for our analyses are listed in Table I. In particular, we use an optical depth τ that is produced as an output by our 21-cm simulations; it is then used to compute the CMB power spectrum for our CMB analyses.

The fiducial astrophysical parameters we use for our cosmic dawn analyses are listed in Table II. We consider two scenarios: popII-only and popII+popIII. The popII-only scenario, in which the evolution of T_s is driven by atomic-cooling galaxies, is used in the official

HERA analysis pipeline [51, 52]; therefore, we consider it to be our baseline. Including popIII stars, which are sourced by molecular cooling galaxies inside mini-halos with $M_h \lesssim 10^8\,M_\odot$ [118, 127, 128], anticipates reionization, and τ shifts to ~ 0.05 in the SIν model and to ~ 0.07 in the others. The addition of popIII stars also increases the number of parameters, so the analysis is subject to larger uncertainties and is computationally more expensive. Nevertheless, the abundance of mini-halos strongly depends on the shape of $P_m(k, z)$ on very small scales, so we expect the inclusion of popIII stars to affect the constraining power of HERA data [53], particularly for the MIν model. Therefore, we also analyze a popII+popIII scenario.

2. Optical depth computation

The optical depth τ is the line-of-sight integral of the mean electron density $\bar{n}_e(z)$ and is given by [45, 46]

$$
\tau = \frac{\sigma_T \, 3H_0^2 \Omega_b}{8\pi G m_p} \left[1 + \frac{Y_p^{\mathrm{BBN}}}{4} \left(\frac{m_{\mathrm{He}}}{m_{\mathrm{H}}} - 1 \right) \right]^{-1} \times \\
\times \int_0^{z_{\mathrm{CMB}}} dz \, \frac{c(1+z)^2}{H_0 \sqrt{\Omega_m(1+z)^3 + \Omega_\Lambda}} \overline{x_{\mathrm{HII}}(1 + \delta_b)},
\tag{21}
$$

where σ_T is the Thompson cross-section, $m_{\mathrm{p,H,He}}$ are the proton mass and the atomic masses for H and Helium (He), respectively, and Y_p^{BBN} is the primordial He mass fraction. We can estimate τ and its uncertainty based on the other cosmological parameters and the density-weighted ionization fraction $\overline{x_{\mathrm{HII}}(1 + \delta_b)}$ [45, 46]. This latter quantity is approximately ~ 1 for $z \lesssim 5$ when the Universe is fully ionized and ~ 0 for $z \gtrsim 35$ before reionization; its value during cosmic dawn and the epoch of reionization can instead be directly estimated from our `21cmFirstCLASS` simulations. The resulting value of τ for each of our fiducial models in Table I is consistent with the cosmological and astrophysical model in the simulation. In our analysis in Sec. IV B, the uncertainty on τ is inferred from the uncertainties on the other parameters.

A. Detector specifications

The sensitivity of detectors measuring the 21-cm signal or the CMB has been widely discussed in the literature. Here, we summarize the main ingredients needed for our forecasts.

1. Cosmic dawn: HERA

To explore the constraining power of the 21-cm signal during cosmic dawn, we consider the design sensitivity of HERA [48], which is expected to be achieved in the reasonably near future. It is composed of ~ 330 packed antennas, distributed in a hexagonal shape with $14\,\mathrm{m}$ diameter dishes. The observational frequency band ranges
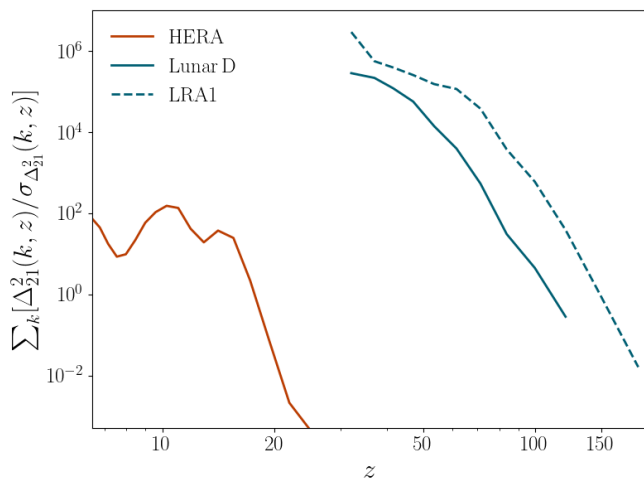
FIG. 8. Cumulative SNR as a function of z for the 21-cm experiments considered in this work. HERA probes the era of cosmic dawn, while Lunar D and LRA1 are configurations to probe the dark ages.

between 50 and 250 MHz, with a resolution 8 MHz and 82 channels probing each bandwidth. The 21-cm signal is divided into ~ 25 bins between $z \sim [5, 27]$. The bins are equally spaced in frequency, while their width varies in redshift. We assume $t_o \simeq 3000$ hr integration time (540 days). The detector properties are summarized in Table III.

We estimate the sensitivity $\sigma_{\Delta^2_{21}, \mathrm{CD}}$ using the public code `21cmSense`[6] [129–131]. The code allows us to account for cosmic variance, instrumental noise, and foreground reduction. In particular, we assume the so-called *moderate scenario* [130], in which the foreground-contaminated wedge on the line-of-sight modes $k_\parallel$ extends $0.1\, h\mathrm{Mpc}^{-1}$ beyond the detector horizon [132].

Figure 8 shows the redshift-dependent cumulative signal-to-noise ratio

$$\mathrm{SNR}(z) = \sum_{k \in k_{\mathrm{HERA}}} \frac{\Delta^2_{21}(k, z)}{\sigma_{\Delta^2_{21}, \mathrm{CD}}(k, z)} \qquad (22)$$

for HERA, obtained using `21cmSense` and summing over the scale range $k_{\mathrm{HERA}} \in [0.05, 1.5]\,\mathrm{Mpc}^{-1}$ allowed by the instrument resolution.

2. Dark ages: Lunar arrays

Finally, we explore the prospects of measuring the 21-cm signal deep in the dark ages. The SKAO or any other ground-based detector can only slightly extend the low-frequency range observed by HERA because of atmospheric effects. Hence, a new observational window can

be opened by constructing an array in a location with no atmosphere, such as the Lunar far side, which would also use the Moon to shield radio interference from Earth (e.g., Refs. [55, 57–59]).

We provide an order-of-magnitude estimate of the noise that such detectors could reach. Following Refs. [133–135] (see also Refs. [136–138] for further details on the 21-cm noise computation), we model the noise $\sigma_{\Delta^2_{21}, \mathrm{DA}}(k, z)$ as the sum between the thermal noise

$$\Delta^2_N(k, z) = \frac{2}{\pi} \sqrt{\frac{k^3 V_z}{\Delta \ln k}} \frac{T^2_{\mathrm{sys}}}{\delta\nu\, t_o} \frac{1}{N_{\mathrm{ant}}} \qquad (23)$$

and the sample variance

$$\Delta^2_{CV}(k, z) = \frac{2\pi \Delta^2_{21}(k, z)}{\sqrt{V_z k^3 \Delta \ln k}}, \qquad (24)$$

which we set equal to the signal mean in the Poisson approximation. The observed volume is $V_z = 4\pi f_{\mathrm{sky}} \chi^2(z) \Delta\chi(z)$, where $\chi(z)$ is the comoving distance to the center of each redshift bin z_i, and $\Delta\chi = \chi(z^i_{\mathrm{max}}) - \chi(z^i_{\mathrm{min}})$ is its width. We set the observed sky fraction to $f_{\mathrm{sky}} = 0.75$ and the system temperature to the sky temperature $T_{\mathrm{sys}} \sim T_{\mathrm{sky}} = 180\,\mathrm{K}(\nu/180\,\mathrm{MHz})^{-2.6}$, neglecting the contribution of the instrument.

In our dark ages forecast, we consider two different detector configurations: Lunar D (based on the D scenario in the Supplementary Material of Ref. [135]) and LRA1 (based on the lunar radio array in Refs. [139–142]). For Lunar D, we use 10 frequency bins between 10 MHz and 45 MHz, with frequency resolution $\delta\nu = 5$ MHz. These choices correspond to $z \sim [30, 150]$, with bins between $z^i_{\mathrm{min,max}} = -1 + \nu_{21}/(\nu^i_{\mathrm{obs}} \pm \delta\nu/2)$. For LRA1, we use 40 bins between 6.3 MHz and 46.3 MHz (corresponding to $z \sim [30, 220]$), with frequency resolution $\delta\nu = 1$ MHz.

For both configurations, we set the total observation time to $t_o = 10^4$ hr. We estimate the number of dipole-like antennas to be [143]

$$N_{\mathrm{ant}} = \frac{f_{\mathrm{cover}} \pi D^2_{\mathrm{base}}/4}{A_{\mathrm{eff}}}, \qquad (25)$$

where D_{base} is the maximum baseline of the experiment, f_{cover} is the fraction of interferometer area covered by antennas, and A_{eff} is the effective collecting area of the dipoles. We estimate $A_{\mathrm{eff}} = G(21\,\mathrm{cm})^2(1 + 50)^2/4\pi$ with $G = 1.64$. Therefore, in our analyses we consider $\{D_{\mathrm{base}}, f_{\mathrm{cover}}, N_{\mathrm{ant}}\} = \{20\,\mathrm{km}, 0.2, 4\times10^6\}$ for Lunar D and $\{100\,\mathrm{km}, 0.2, 1\times10^8\}$ for LRA1. All detector properties are summarized in Table III.

Finally, we set $\Delta \ln k = 0.5$ and define $k_{\mathrm{min}} = 2\pi/L_{\mathrm{box}}$ and k_{max} as the maximum between the scale probed by the resolution of the simulation, $2\pi N_{\mathrm{cell}}/L_{\mathrm{box}}$, and the resolution of the detector, $2\pi D_{\mathrm{base}}/[21\,\mathrm{cm}(1 + z)\chi(z)]$. For example, at $z = 30$, we have $k_{\mathrm{max}} \simeq 1.5\,\mathrm{Mpc}^{-1}$ for Lunar D and $k_{\mathrm{max}} \simeq 8\,\mathrm{Mpc}^{-1}$ for LRA1; therefore, for Lunar D, we derive our results using the same `21cmFirstCLASS` simulation adopted for cosmic dawn,

	$\Delta\nu$ [MHz]	$\delta\nu$ [MHz]	N_{ant}	t_o [hr]	Ref.
HERA	[50, 250]	8	330 dishes	3000	[129, 130]
Lunar D	[10, 45]	5	4×10^6 dipoles	10^4	[135]
LRA1	[6.3, 46.3]	1	1×10^8 dipoles	10^4	[140–142]

TABLE III. Specifications for the 21-cm detectors used in our analyses. We list the observed frequency range $\Delta\nu$, frequency resolution $\delta\nu$, type and number of antennas N_{ant}, and observation time t_o.

while for LRA1 we add the information on scales $k > 1.5\,\mathrm{Mpc}^{-1}$ from the smaller simulation introduced in at beginning of Sec. IV.

Figure 8 compares the performance of the two Lunar setups with HERA. Although the Lunar detector is more futuristic, we see that it would allow us to probe a completely different regime of cosmic history, where the cosmological signal is pristine: it is in the linear regime with no astrophysical contamination.

3. CMB-S4

For the CMB analysis, we adopt the latest specifications of the wide survey proposed for CMB-S4. We use noise curves from the *CMB-S4: Dark Radiation Anisotropy Flowdown Team (DRAFT) tool*[7], for the *S4-wide Chilean LAT configuration*[8], updated on October 2023 [144–147]. Here, the observed sky fraction is $f_{\mathrm{sky}} = 0.6$, and the properties of the detector are combined separately for TT and EE to get the noise power spectra

$$N_\ell^{T,E} = \Delta_{T,E}^2[\mathrm{rad}]\exp\left(\ell(\ell+1)\frac{\theta_{\mathrm{FWHM}}[\mathrm{rad}]}{\sqrt{8\log(2)}}\right) \times \left[1 + (\ell\ell_{\mathrm{knee}}^{T,E})^{\alpha_{T,E}}\right]. \quad (26)$$

We use the 93 GHz channel, for which the angular resolution is $\theta_{\mathrm{FWHM}} = 2.2\,\mathrm{arcmin}$, and the instrumental noises are $\Delta_T = 2\,\mu\mathrm{K/arcmin}$ and $\Delta_E = 2.68\,\mu\mathrm{K/arcmin}$. Additionally, $[\ell_{\mathrm{knee}}^T, \alpha_T] = [1932, 3.5]$ and $[\ell_{\mathrm{knee}}^E, \alpha_E] = [700, 1, 4]$. We restrict our analysis to multipoles $\ell \in [30, 3000]$.

We could improve sensitivity, for example, by implementing a cross-internal linear combination approach [144] or using a forecast-loop pipeline [148]. These approaches can further improve the constraining power on the small scales by reducing the contamination of astrophysical signals; their implementation, however, is beyond the scope of this work.

---

[7] https://github.com/sriniraghunathan/DRAFT/tree/master
[8] https://github.com/sriniraghunathan/DRAFT/tree/master/products/202310xx_PBDR_config/s4wide_202310xx_pbdr_config

B. Fisher matrix formalism

We use the Fisher matrix formalism to perform our forecasts (see, e.g., Ref. [149] for review). Our baseline cosmological parameters and their fiducial values are listed in Table I. We have the six vanilla ΛCDM cosmological parameters and the three parameters that characterize the neutrino properties: G_{eff}, M_ν, and N_{eff}. We also include the full set of astrophysical parameters listed in Table II.

For each self-interacting neutrino model (SI_ν, MI_ν, mI_ν) and each astrophysical scenario (popII, popII+popIII), we estimate the numerical derivatives of $\Delta_{21}^2(k,z)$ with respect to all parameters using different realizations of 21cmFirstCLASS. Since the optical depth τ does not influence either the shape or the amplitude of the 21-cm power spectrum, we have $d\Delta_{21}^2/d\tau = 0$, indicating that τ cannot be constrained through the 21-cm signal alone. However, as discussed in Sec. IV 2, the value of τ at cosmic dawn directly depends on the ionization fraction x_{HII}; hence, we estimate it from the output of our 21cmFirstCLASS simulations.

Using the $\sigma_{\Delta_{21}^2,(\mathrm{CD,DA})}(k,z)$ sensitivities estimated by 21cmSense for cosmic dawn or from Eqs. (23) and (24) for the dark ages, the Fisher matrices for HERA and Lunar D are

$$F_{21,\alpha\beta}^{(\mathrm{CD,DA})} = \sum_{z,k}\frac{1}{\sigma_{\Delta_{21}^2,(\mathrm{CD,DA})}^2(k,z)}\frac{d\Delta_{21}^2(k,z)}{d\theta_\alpha}\frac{d\Delta_{21}^2(k,z)}{d\theta_\beta}. \quad (27)$$

Finally, forecasts for LRA1 are obtained by summing two Fisher matrices: one estimated from the same simulation box as the other detectors and another from the small, high-resolution box. To avoid double counting when summing over k, we use the larger box up to $k = 1\,\mathrm{Mpc}^{-1}$ and the smaller box to account for larger k. The 1σ uncertainty for each cosmological or astrophysical parameter θ_i is obtained from the diagonal elements of the inverse Fisher matrices:

$$\sigma_{\theta_i,(\mathrm{CD,DA})} = \sqrt{\left(F_{21}^{(\mathrm{CD,DA})}\right)_{ii}^{-1}}. \quad (28)$$

We construct the CMB-S4 Fisher matrix for each model of interest by running nuCLASS to get the covariance and the derivatives of $C_\ell^{TT,TE,EE}$ with respect to the cosmological parameters. We choose the same step sizes for the computation of the 21-cm and CMB numerical derivatives. In this case, the Fisher matrix is

$$F_{\mathrm{CMB},\alpha\beta} = f_{\mathrm{sky}}\sum_\ell\frac{2\ell+1}{2}\mathrm{Tr}\left[\mathbf{C}_\ell^{-1}\frac{d\mathbf{C}_\ell}{d\theta_\alpha}\mathbf{C}_\ell^{-1}\frac{d\mathbf{C}_\ell}{d\theta_\beta}\right] \quad (29)$$

where the $\mathbf{C}_\ell$ matrix is defined by the signal and noise contributions in the TT, TE, and EE channels:

$$\mathbf{C}_\ell = \begin{pmatrix} C_\ell^{TT} + N_\ell^{TT} & C_\ell^{TE} \\ C_\ell^{TE} & C_\ell^{EE} + N_\ell^{EE} \end{pmatrix}. \quad (30)$$

	SIν	MIν	mIν
$\log_{10} G_{\mathrm{eff}}$ fiducial value	-1.77	-4	-5
CMB-S4	14%	66%	534%
HERA (cosmic dawn)	32%	16%	112%
HERA + CMB-S4	8%	11%	12%
Lunar D (dark ages)	14%	42%	240%
LRA1 (dark ages)	1%	2%	5%
Lunar D + CMB-S4	5%	19%	123%
LRA1 + CMB-S4	1%	1%	4%

TABLE IV. Summary of the main results of our paper. We provide forecasts for the 2σ uncertainties on the (log of the) neutrino self-coupling strength $\log_{10}(G_{\mathrm{eff}}/\mathrm{MeV}^{-2})$, for strong (SI$\nu$), moderate (MI$\nu$), and mild (mI$\nu$) self-interaction models; see Table I. The MIν and mIν models are at the cusp or beyond the reach, respectively, of current CMB experiments. The results for the cosmic dawn analyses use the popII astrophysical model in Table II.

Again, we obtain the 1σ uncertainty from the diagonal elements of the inverted Fisher matrix

$$\sigma_{\theta_i,\mathrm{CMB}} = \sqrt{(F_{\mathrm{CMB}})_{ii}^{-1}}. \quad (31)$$

Since we are using a single channel and a restricted range $\ell \in [30, 3000]$, our forecasts are conservative.

Finally, we combine the 21-cm and CMB Fisher matrices to help break parameter degeneracies. For the dark ages, we use the matrix $F_{\mathrm{tot}}^{DA} = F_{\mathrm{CMB}} + F_{21}^{\mathrm{DA}}$. For cosmic dawn, we must account for the propagation of uncertainties in the modeling of τ in Sec. IV 2. Following Refs. [45, 46], we first compute $F_{\mathrm{tot}}^{\mathrm{CD}} = F_{\mathrm{CMB}} + F_{21}^{\mathrm{CD}}$ (including all astrophysical and cosmological parameters) and then define

$$\tilde{F}_{\mathrm{tot},ij}^{\mathrm{CD}} = F_{\mathrm{tot},ij}^{\mathrm{CD}} + a_i F_{\mathrm{tot},j\tau}^{\mathrm{CD}} + a_j F_{\mathrm{tot},i\tau}^{\mathrm{CD}} + a_i a_j F_{\mathrm{tot},\tau\tau}^{\mathrm{CD}}. \quad (32)$$

In $\tilde{F}_{\mathrm{tot}}^{\mathrm{CD}}$ there are no rows and columns related to τ, and for each parameter θ_i, the factor $a_i = d\tau/d\theta_i$ is estimated from the different realizations of the `21cmFirstCLASS` simulation. The uncertainty in the optical depth is then computed by drawing random samples of all the other parameters θ_i from Gaussian distributions centered around their fiducial values with a standard deviation $\sigma_{\mathrm{tot},\theta_i} = \sqrt{(\tilde{F}_{\mathrm{tot}}^{\mathrm{CD}})_{ii}^{-1}}$. Thus, for each sample, we estimate the optical depth as $\tilde{\tau} = \sum_{\theta_i} a_i \theta_i$, and we set the uncertainty $\sigma_{\mathrm{tot},\tau}$ to be equal to the spread between the different values of $\tilde{\tau}$.

V. RESULTS

Our goal in this work is to understand if and how well upcoming 21-cm and CMB data can probe models of self-interacting massive neutrinos. The main results of our

Fisher analyses are summarized in Table IV: we provide forecasts for the 2σ uncertainty on the self-interaction coupling strength $\log_{10}(G_{\mathrm{eff}}/\mathrm{MeV}^{-2})$ for the three self-interacting neutrino models of interest, using the popII astrophysical model in Table II as our baseline for the cosmic dawn analysis. Figure 9 shows the forecasts for M_ν and $\log_{10} G_{\mathrm{eff}}$, marginalizing over all other cosmological and astrophysical parameters, for CMB and 21-cm cosmic dawn.

The full triangle plot for mIν with all cosmological and astrophysical parameters for the analyses involving 21-cm cosmic dawn is shown in Fig. 12 in Appendix C. The full triangle plots for mIν with all cosmological parameters for the Lunar D and LRA1 analyses are shown in Fig. 13 in Appendix C. All triangle plots in Appendix C also include the joint analysis with CMB-S4.

1. CMB-S4 forecasts

We have validated our pipeline by running the Fisher matrix analysis for the ΛCDM+N_{eff} + M_ν cosmology, with no self-interacting neutrinos. Our results on the neutrino parameters are broadly in agreement with forecasts in the CMB-S4 Science Book [150].

Regarding the constraints on $\log_{10} G_{\mathrm{eff}}$ for self-interacting neutrinos, Ref. [32] performed a similar forecast analysis. However, that work considered three massless self-interacting neutrinos with a fiducial of $\log_{10} G_{\mathrm{eff}} = -1.92$, matching the best fit obtained in Ref. [31] using *Planck* 2018 TT+TE+EE+lowE data. Compared to our work here, Ref. [31] adopts a slightly different definition of $\log_{10} G_{\mathrm{eff}}$, which is in line with Ref. [24]. The noise treatment is also slightly different from ours. Their forecast uncertainty is $2\sigma_{\log_{10} G_{\mathrm{eff}}} \simeq 10\%$, close to our value in Table I. We have verified that assuming $M_\nu = 0$ and changing the $\log_{10} G_{\mathrm{eff}}$ fiducial value and noise accordingly, the difference between our result and theirs reduces.

Reference [31] also found an upper limit on a moderate interaction at $\log_{10} G_{\mathrm{eff}} = -4.05$, with $2\sigma_{\log_{10} G_{\mathrm{eff}}} = 50\%$ from *Planck*+ACT data [151]. This result is consistent with ours for MIν from CMB-S4 alone. For the smaller interaction of the mIν model, our result indicates that the bound from CMB-S4 would be very weak.

2. HERA forecasts

HERA provides better sensitivity over CMB-S4 to $\log_{10} G_{\mathrm{eff}}$ for the MIν model. The constraining power arises from the indirect sensitivity to the matter power spectrum at small scales: the enhancement bump increases the abundance of the small- and intermediate-mass halos that host the galaxies that dominate the evolution of the 21-cm signal during cosmic dawn. This result opens the possibility of exploring a new region of the parameter space, which so far has been inaccessible using CMB primary anisotropies and galaxy surveys.
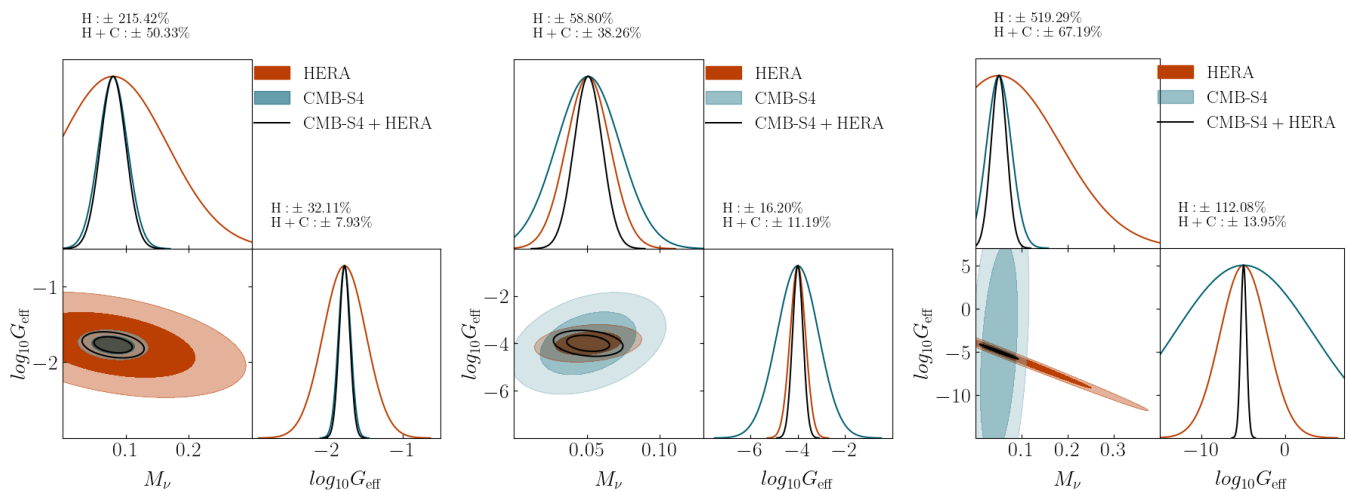
FIG. 9. Summary plot of the main results of our paper. We show forecasts for the constraining power of $\Delta_{21}^2(k,z)$ during cosmic dawn on the sum of neutrino masses M_ν and the neutrino self-interaction coupling strength $\log_{10} G_{\rm eff}\,[{\rm MeV}^{-2}]$ in the case of strong (left), moderate (center) and mild interaction (right). The analysis has been run on the full set of parameters listed in Tables I and II, and then marginalizing with uninformative priors over all but the two parameters shown. The 21-cm measurement from HERA can provide stronger constraints over CMB-S4 for the MIν model, though our projections for CMB-S4 are conservative. For the mIν model, the individual experiments have poor constraining power, but the joint analysis of HERA and CMB-S4 breaks the degeneracy between $\log_{10} G_{\rm eff}$ and M_ν, providing a significant improvement. See also Table IV.

Although HERA also outperforms CMB-S4 in constraining $\log_{10} G_{\rm eff}$ for the mIν model, the right panel of Fig. 9 shows that HERA is limited by the anti-correlation with M_ν. Increasing $\log_{10} G_{\rm eff}$ makes it easier to form halos in the relevant M_h range, which speeds up the evolution of $T_{21}(z)$ and leads to a smaller $\Delta_{21}^2(k,z)$ for $k \sim [0.1, 0.5]\,{\rm Mpc}^{-1}$, where HERA is sensitive.[9] The same effect would still occur if M_ν were smaller than our fiducial choice, thus explaining the anti-correlation. In other words, lighter neutrinos would compensate for the effect of mIν on $\Delta_{21}^2(k,z)$.

A very interesting possibility to further improve the constraining power is to combine 21-cm and CMB datasets. Table IV highlights the great potential that joint CMB and 21-cm cosmic dawn analyses have for self-interacting massive neutrinos. Under all three self-interaction models, the joint analysis reduces the uncertainty on $\log_{10} G_{\rm eff}$ to $\sim 10\%$. As shown in Fig. 9, the combination of CMB and 21-cm is crucial for breaking the degeneracy between neutrino parameters, as well as other degeneracies that may exist within the parameter set, as highlighted in Fig. 12. Incorporating 21-cm data from the cosmic dawn helps mitigate the degeneracy between M_ν, τ, and A_s; in this context, we have verified that our analysis returns a comparable result with the

analysis in Ref. [46]. There is also a slight improvement of the constraining power on the astrophysical parameters.

Thus far, the discussion of our results has focused on our baseline astrophysical scenario, where only popII stars are included. We now consider what happens when we include popIII stars in the analysis. Having been formed in mini-halos, popIII stars indirectly probe the small-scale regime, $k \gtrsim 30\,{\rm Mpc}^{-1}$ (compare with Fig. 5). In the mIν and MIν models, these scales are boosted; hence, the number of mini-halos is strongly enhanced, anticipating the onset of cosmic dawn and increasing the amplitude of the 21-cm power spectrum at high z. Meanwhile, the suppression of small scales in the SIν model weakens the amplitude of the 21-cm power spectrum; this suppression, in addition to the larger number of parameters needed to analyze the popII+popIII scenario, worsens the constraining power of $\Delta_{21}^2(k,z)$.

To help visualize this point, we compare the only-popII and popII+popIII scenarios in Fig. 10, where the HERA results for only-popII are the same from Fig. 9. The enhanced small-scale power in the mIν model helps to relax the degeneracy between M_ν and $\log_{10} G_{\rm eff}$, improving the constraining power on the latter; the $2\sigma_{\log_{10} G_{\rm eff}}$ constraints from Table IV, in fact, shift from 112% to 78%. In contrast, the constraints on the SIν model are weaker when popIII stars are included in the analysis, with $2\sigma_{\log_{10} G_{\rm eff}}$ shifting from 32% to 72%.

Finally, we note that variations in the fiducial astrophysical model may vary the evolution of the 21-cm signal (see, e.g., Refs. [94, 152, 153]). This may affect our final results, since the 21-cm power spectrum would shift in redshift, with cosmic dawn being either anticipated or

---

[9] It may seem counterintuitive that a larger HMF leads to a smaller $\Delta_{21}^2(k,z)$. Recall that the amplitude of the 21-cm signal depends not just on the abundance of the astrophysical sources, but also on the interplay of their radiation fields, the way they heat and ionize the gas, etc. In particular, having more galaxies at $z = 13$ implies producing more X-rays, so $T_{\rm gas}$ and T_s get closer to the CMB temperature, thereby decreasing T_{21}.
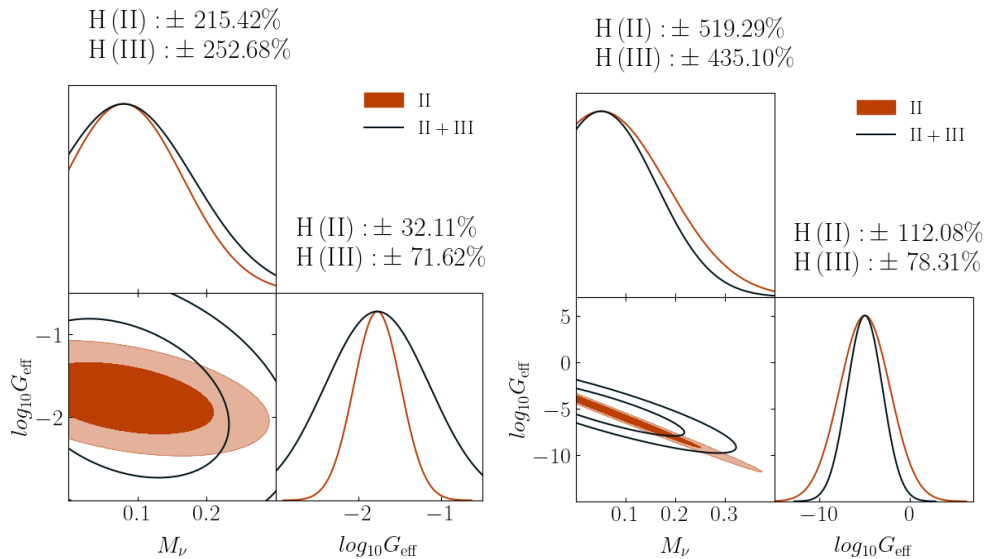
FIG. 10. Forecasts for the constraining power of HERA for the SIν (left) and mIν (right) models, using the only-popII (red) and popII+popIII (black) scenarios. The numbers above each panel indicate 2σ constraints.

delayed, hence changing the sensitivity of HERA to its amplitude on the different scales. However, since none of these parameters can introduce scale-dependent effects, we expect the constraining power on G_{eff} to remain in the same ballpark. For example, a smaller value of $f_{*,7}$, the popIII star formation efficiency, would lead to $\sigma_{\log_{10} G_{\text{eff}}}$ in between the values we quoted for the two scenarios.

3. Lunar array forecasts

Lunar detectors can probe neutrino properties more directly: there are no astrophysical sources during the dark ages and thus the 21-cm signal is shaped by only the cosmological parameters. Their great advantage comes from their capability of accessing very small scales, which could be of particular interest for the MIν and mIν models. As shown in Fig. 2, these models feature a boost in $P_m(k,z)$ for $k \in [0.1, 10]\,\text{Mpc}^{-1}$. While these scales are outside the reach of Lunar D, they do fall within some of the redshift bins of LRA1.

We show in Fig. 11 the confidence ellipses for the mIν model on the neutrino parameters M_ν and $\log_{10} G_{\text{eff}}$; the two panels correspond to the Lunar D and LRA1 experimental configurations, respectively. These plots, together with the results in Table IV, show that LRA1 could reach a strong detection of neutrino self-interactions, even for quite small values of the coupling strength. The ability of LRA1 to reach very small scales is the key to constraining not only $\log_{10} G_{\text{eff}}$, but all the other cosmological parameters as well; this is evident by looking at the confidence ellipses on the full set of parameters in Fig. 13.

Comparing the performances of the two experiments in Figs. 11 and 13, in fact, we notice that the confidence ellipses in the LRA1 case show fewer degeneracies

among parameters (e.g., between h and Ω_c or between M_ν and A_s), which leads to better constraints on the full parameter set. For the same reason, combining LRA1 with CMB-S4 does not improve the constraining power on $\log_{10} G_{\text{eff}}$ by much. Using CMB-S4 is instead helpful in breaking the internal degeneracies in the Lunar D case, improving its capability of constraining the MIν scenario.

VI. FINAL REMARKS

Alongside traditional methods of studying cosmology, such as CMB observations and galaxy surveys, the exploration of the 21-cm signal from cosmic dawn and the dark ages is expected to become increasingly important in the coming years. This observable will provide a powerful tool, offering insights into cosmological models beyond ΛCDM and extensions to the Standard Model of particle physics.

In this paper, we investigate self-interacting massive neutrinos. We consider the scale-dependent changes in the matter power spectrum that self-interacting neutrinos introduce and how those changes propagate to the 21-cm power spectrum. Scales that enter the horizon before neutrino self-decoupling are damped, while modes entering the horizon around the time of self-decoupling are strongly boosted. The scales on which the boost occurs depend on the coupling strength of the self-interaction, G_{eff}.

We study three fiducial models: massive neutrinos with a strong (SIν), moderate (MIν), and mild (mIν) self-interaction. We explore two astrophysical scenarios for the 21-cm signal from cosmic dawn: one in which star formation is driven solely by population II stars within atomic cooling galaxies, and another that also includes
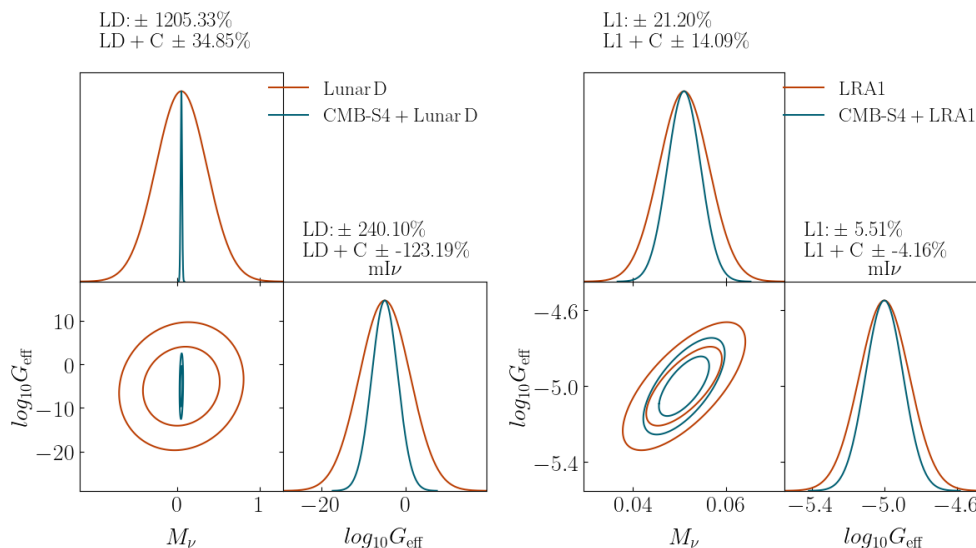
FIG. 11. Confidence ellipses on the neutrino parameters for Lunar D (left) and LRA1 (right) for the mIν model. We consider the experiments alone (red) or in combination with CMB-S4 (blue). The numbers above each panel indicate 2σ constraints.

the effect from population III stars within molecular cooling galaxies, associated with high-redshift mini-halos. Finally, we perform Fisher forecasts to analyze various experimental setups involving separate and joint analyses for CMB and 21-cm experiments. We consider CMB-S4, HERA for the 21-cm cosmic dawn signal, and two Lunar configurations for the 21-cm dark ages signal.

We find that the 21-cm signal during the cosmic dawn provides an indirect way to investigate physics that impacts small-scale structure, due to the interplay between the halo mass function (whose shape depends on the matter power spectrum) and the star formation rate density. Galaxies that mainly drive cosmic dawn evolution are hosted by halos in the $10^9 - 10^{11}\,M_\odot$ mass range, whose abundance is determined by $P_m(k,z)$ on $k \sim 1 - 100\,\mathrm{Mpc}^{-1}$. This range of scales, that are just beyond the reach of current CMB observations, is precisely where neutrino self-interactions could play a role.

A key finding in our work is that joint CMB and 21-cm analyses can provide a substantial improvement in constraining power over an individual analysis of either alone. The CMB and 21-cm power spectra access different cosmic scales, so together they are a powerful probe of correlated physics that span a wide range in k. Their combination can break internal degeneracies among parameters, allowing one probe to tightly constrain neutrino properties more directly, while the other probe helps by constraining other parameters in the joint analysis interchangeably. For example, as Refs. [45, 46] have shown in the context of ΛCDM, the 21-cm signal can be used to mitigate the $M_\nu - \tau - A_s$ degeneracy in CMB studies; in our case, it also leads to improving the constraints on the self-interaction.

During the dark ages, the 21-cm power spectrum carries pristine information about cosmology. Even if challenging, we find that observing the 21-cm signal in this epoch can provide very strong constraints on the cosmological parameters that affect the shape of the matter power spectrum.

To conclude, our results highlight the unique potential of the 21-cm power spectrum in probing new physics beyond ΛCDM and beyond the SM. By complementing traditional observables such as the CMB, 21-cm measurements can play a key role in constraining self-interacting massive neutrinos, as well as other beyond-SM scenarios, shedding light on fundamental physics on previously inaccessible scales.

ACKNOWLEDGMENTS

Appendix A: Modified Boltzmann equations for neutrino self-interaction

In this section, we describe the modifications of the Boltzmann equations implemented in CLASS which we have made publicly available in the code nuCLASS. We sketch our modifications, which follow Ref. [28].

The low-energy neutrino interaction Lagrangian in the presence of a scalar mediator φ of mass m_φ is given by

$$\mathcal{L} \supset g_{\nu,ij}\varphi\bar{\nu}_i\nu_j \;, \tag{A1}$$

where ν_i is the left-handed neutrino spinor of flavor i. In this work, we consider flavor-universal interactions and set the coupling

$$g_{\nu,ij} = g_\nu\delta_{ij} \;, \tag{A2}$$

where δ_{ij} is the Kronecker delta function and g_ν is the universal coupling. The scattering matrix element for 4-neutrino scattering in the presence of the interaction is

$$|\mathcal{M}|^2 = \sum_{\text{spin}} |\mathcal{M}|^2_{\nu_i+\nu_j\to\nu_k+\nu_l} \tag{A3}$$

$$= 2G^2_{\text{eff}}(s^2 + t^2 + u^2) \;, \tag{A4}$$

where s, t and u are the Mandelstam variables and $G_{\text{eff}} = g_\nu^2/m_\varphi^2$ as in Eq. (2).

The perturbed neutrino distribution function is

$$f_\nu(\mathbf{x}, \mathbf{p}, \tau) = f_\nu^{(0)}(p, \tau)[1 + \Psi(\mathbf{x}, \mathbf{p}, \tau)] \;, \tag{A5}$$

where $\mathbf{x}$ is a spatial coordinate, $\mathbf{p}$ is the proper momentum with magnitude $p = |\mathbf{p}|$, and τ is conformal time. The background neutrino distribution function is taken to be Fermi-Dirac:

$$f_\nu^{(0)}(p, \tau) = \frac{1}{e^{p/T_\nu} + 1} \;, \tag{A6}$$

where T_ν is the neutrino temperature. The perturbation $\Psi(\mathbf{k}, \mathbf{p}, \tau)$ encodes the inhomogeneities in the neutrino distribution function in the conjugate-momentum space, and it is expanded into multipole moments in the following manner [83]:

$$\Psi(\mathbf{k}, \mathbf{p}, \tau) = \sum_{\ell=0}^\infty (-i)^\ell (2\ell+1)\Psi_\ell(k, p, \tau)P_\ell(\mu) \;, \tag{A7}$$

where $P_\ell(\mu)$ is the Legendre polynomial with $\mu = \hat{k}\cdot\hat{p}$. The momentum-dependent Boltzmann equation in the presence of the interaction is

$$\dot{\Psi}_\ell + k\frac{q}{\epsilon}\left(\frac{\ell+1}{2\ell+1}\Psi_{\ell+1} - \frac{\ell}{2\ell+1}\Psi_{\ell-1}\right)$$
$$+ \left(\dot{\phi}\delta_{\ell0} + \frac{k\epsilon}{3q}\psi\delta_{\ell1}\right)\frac{d\ln f_\nu^{(0)}}{d\ln q}$$
$$= -aG^2_{\text{eff}}T_\nu^5\left(\frac{1}{f_\nu^{(0)}}\frac{T_{\nu,0}}{q}\right)\times$$
$$\left[A\left(\frac{q}{T_{\nu,0}}\right) + B_\ell\left(\frac{q}{T_{\nu,0}}\right) - 2D_\ell\left(\frac{q}{T_{\nu,0}}\right)\right]\Psi_\ell \;, \tag{A8}$$

where the overdot (˙) denotes a derivative with respect to τ, $q \equiv ap$ is the comoving momentum, $\epsilon = \sqrt{q^2 + a^2m_\nu^2}$, m_ν is the neutrino mass, ϕ and ψ are Newtonian potentials, a is the scale factor, and $T_{\nu,0}$ is the temperature of neutrinos today ($a = 1$). Due to the conservation of number density (i.e., detailed balance) for elastic scattering, we have

$$A(x) + B_0(x) - 2D_0(x) = 0 \;, \tag{A9}$$

where $x \equiv q/T_{\nu,0}$. Since neutrinos self-scatter, there is a conservation of total momentum in the neutrino sector, which results in

$$A(x) + B_1(x) - 2D_1(x) = 0 \;. \tag{A10}$$

We precompute the combination

$$S_l(x) = \frac{1}{xf_\nu^{(0)}}\left[A(x) + B_\ell(x) - 2D_\ell(x)\right] \;, \tag{A11}$$

for different x and ℓ values and store the results as an interpolation file to be used for nuCLASS computations.

The functions A, B_ℓ, and C_ℓ associated with the collision term are as follows:

$$A(x_1) = \frac{1}{8\pi^3}\int_0^\infty \frac{e^{x_2}dx_2}{e^{x_2}+1}\int_0^{x_1+x_2}\frac{x_3dx_3}{(e^{x_3}+1)(e^{x_1+x_2-x_3}+1)}\int_{\text{Max}[\eta_-,1]}^1\frac{|\bar{\mathcal{M}}_\eta(x_1,x_2,x_3,\eta)|^2}{\sqrt{x_1^2+x_3^2-2x_1x_3\eta}}d\eta \;, \tag{A12}$$

$$B_\ell(x_1) = \frac{1}{8\pi^3 x_1}\int_0^\infty \frac{x_2^2 e^{x_2}dx_2}{e^{x_2}+1}\int_0^{x_1+x_2}\frac{dx_3}{(e^{x_3}+1)(e^{x_1+x_2-x_3}+1)}\int_{\text{Max}[\rho_-,1]}^1\frac{|\bar{\mathcal{M}}_\rho(x_1,x_2,x_3,\rho)|^2 P_\ell(\rho)}{\sqrt{x_1^2+x_2^2+2x_1x_2\rho}}d\rho \;, \tag{A13}$$

$$D_\ell(x_1) = \frac{e^{-x_1}}{8\pi^3 x_1}\int_0^\infty \frac{dx_2}{e^{x_2}+1}\int_0^{x_1+x_2}\frac{e^{x_3}x_3^2 dx_3}{(e^{x_3}+1)(e^{-(x_1+x_2-x_3)}+1)}\int_{\text{Max}[\eta_-,1]}^1\frac{|\bar{\mathcal{M}}_\eta(x_1,x_2,x_3,\eta)|^2 P_\ell(\eta)}{\sqrt{x_1^2+x_3^2-2x_1x_3\eta}}d\eta \;, \tag{A14}$$

where

$$|\bar{\mathcal{M}}_\eta(x_1, x_2, x_3, \eta)|^2 = \Delta_{2,\eta}\frac{3b_\eta^2 - 4a_\eta c_\eta}{8a_\eta^2} - \Delta_{1,\eta}\frac{b_\eta}{2a_\eta} + \Delta_{0,\eta} \tag{A15}$$

$$a_\eta = -x_2^2(x_1^2 + x_3^2 - 2x_1 x_3 \eta) \tag{A16}$$

$$b_\eta = 2x_2(x_1 - x_2\eta)[x_1 x_2 + x_3(x_1 + x_2) + x_1 x_3 \eta] \tag{A17}$$

$$c_\eta = -[x_1 x_2 - x_3(x_1 + x_2) + x_1 x_3 \eta]^2 + x_2^2 x_3^2(1 - \eta^2) \tag{A18}$$

$$\Delta_{2,\eta} = x_1^2 x_2^2, \tag{A19}$$

$$\Delta_{1,\eta} = x_1^2 x_2(x_3 - 2x_2 - x_3\eta), \tag{A20}$$

$$\Delta_{0,\eta} = x_1^2(x_2^2 - x_2 x_2 + x_3^2) + x_1 x_3 \eta(x_1 x_2 - 2x_1 x_3 + x_1 x_3 \eta) \tag{A21}$$

$$\eta_- = \frac{(x_1 + 2x_2)x_3 - 2x_2(x_1 + x_2)}{x_1 x_3} \tag{A22}$$

$$|\bar{\mathcal{M}}_\rho(x_1, x_2, x_3, \rho)|^2 = \Delta_{2,\rho}\frac{3b_\rho^2 - 4a_\rho c_\rho}{8a_\rho^2} - \Delta_{1,\rho}\frac{b_\rho}{2a_\rho} + \Delta_{0,\rho} \tag{A23}$$

$$a_\rho = -x_3^2(x_1^2 + x_2^2 + 2x_1 x_2 \rho) \tag{A24}$$

$$b_\rho = 2x_3(x_1 + x_2\rho)[x_2 x_3 + x_1(x_3 - x_2) + x_1 x_2 \rho] \tag{A25}$$

$$c_\rho = -[x_2 x_3 + x_1(x_3 - x_2) + x_1 x_2 \rho]^2 + x_1^2 x_3^2(1 - \eta^2) \tag{A26}$$

$$\Delta_{2,\rho} = x_1^2 x_3^2, \tag{A27}$$

$$\Delta_{1,\rho} = x_1^2 x_3(x_2 - 2x_3 - x_2\rho), \tag{A28}$$

$$\Delta_{0,\rho} = x_1^2(x_2^2 - x_2 x_2 + x_3^2) + x_1 x_2 \rho(x_1 x_3 - 2x_1 x_2 + x_1 x_2 \rho) \tag{A29}$$

$$\rho_- = \frac{x_1 x_2 - 2(x_1 + x_2)x_3 + 2x_3^2}{x_1 x_2} . \tag{A30}$$

Appendix B: 21-cm signal modeling

The main observables for studying the 21-cm signal at high z are the brightness temperature $T_{21}(z)$ and its spatial fluctuations, used to estimate the 21-cm power spectrum in Eq. (5). The former is defined in Eq. (4), where $T_{\mathrm{CMB}}(z)$ is the CMB temperature and $T_s(z)$ the spin temperature. While the CMB temperature decreases with redshift due to the expansion of the Universe, $T_{\mathrm{CMB}}(z) \propto (1 + z)$, the evolution of the spin temperature is driven by the coexistence of different processes that excite H in the intergalactic medium (IGM). In thermal equilibrium, we can write

$$T_s^{-1}(z) = \frac{x_{\mathrm{CMB}}T_\gamma^{-1}(z) + x_{\mathrm{coll}}T_k^{-1}(z) + x_\alpha T_\alpha^{-1}(z)}{x_{\mathrm{CMB}}(z) + x_{\mathrm{coll}}(z) + x_\alpha(z)}, \tag{B1}$$

where $T_k(z)$ is the kinetic temperature of the H gas in the IGM, and $T_\alpha(z) \simeq T_k(z)$ [154] is the color temperature of Lyman-α photons (Lyα). The evolution of $T_k(z)$ over cosmic time is found by solving the following differential equation:

$$\begin{aligned}\frac{dT_k}{dz} = &\frac{dt}{dz}\Big[-2H(z)T_k + \frac{2}{3}\frac{T_k}{1+\delta_b}\frac{d\delta_b}{dt} - \frac{T_k}{1+x_e}\frac{dx_e}{dt} \\ &+ \frac{dT_k}{dt}\Big|_{\mathrm{CMB}} + \frac{dT_k}{dt}\Big|_{\mathrm{Xray}}\Big],\end{aligned} \tag{B2}$$

where $dt/dz = -[H(z)(1 + z)^{-1}]$ and we introduced the free-electron fraction $x_e(z) = n_e/(n_{\mathrm{H}} + n_{\mathrm{He}})$, namely the ratio between the electron number density and the total number density of H and helium (He) nuclei. The evolution of $x_e(z)$ in turn can be found solving the coupled differential equation [155]

$$\frac{dx_e}{dz} = \frac{dt}{dz}\left[\frac{dx_e}{dt}\Big|_{\mathrm{reio}} + \mathcal{C}(\beta_{\mathrm{ion}}(1 - x_e) - \alpha_{\mathrm{rec}}n_{\mathrm{H}}x_e^2)\right], \tag{B3}$$

where $dx_e/dt|_{\mathrm{reio}}$ is the reionization rate at late times, $\mathcal{C}$ represents the Peebles coefficient,[10] while α_{rec} is the recombination rate and β_{ion} the early photoionization rate.

_____

[10] The interested reader can read e.g., App. B in Ref. [63] for discussion on the Peebles coefficients.

In Eq. (B2), changes in T_k can be sourced by either heating due to external sources (second line), or by adiabatic cooling/heating (first line), due to the expansion of the Universe (first term), the clustering of matter (second term) and variations in the total baryon number density sourced by reionization/recombination (third term).

Among the external sources, we consider the heating due to absorptions of CMB photons [85, 156–159] and X-rays from astrophysical sources during cosmic dawn. The contribution of the X-ray heating can be estimated based on the X-ray flux [92]

$$J_X(\boldsymbol{x}, \nu) = \int dR \dot{\rho}_*(\boldsymbol{x}, R) \epsilon_X(\nu') e^{-\tau_X}(\nu', R), \quad \text{(B4)}$$

where $\boldsymbol{x}$ is the point (at redshift z) at which the flux is computed and ν the rest-frame frequency of the X-ray radiation. The integral over shells of comoving radius R accounts for radiation sourced from different redshifts z', so that the frequency at $\boldsymbol{x}$ is $\nu' = \nu(1 + z'(R))/R$. The emissivity $\epsilon_X(\nu')$ accounts for the spectral energy distribution in the X-ray band; its value can be related to the value of the $L_{X,10}$/SFR parameter introduced in Sect. III A 2. Finally, $\dot{\rho}_*$ is the star formation rate density discussed in Sect. III A, while $\tau_X(\nu', R)$ the opacity due to the IGM.

Finally, in Eq. (B1), the coefficients $x_{\text{CMB}}(z)$, $x_{\text{coll}}(z)$, $x_\alpha(z)$ represent, respectively, the coupling with CMB (due to the absorption of CMB photons), the collisional coupling (due to collisions between H atoms) and the Lyα coupling (due to the absorption of Lyα photons under the Wouthuysen-Field effect [88, 89, 160]). On one

side, $x_{\text{CMB}}(z) = (1 - e^{\tau_{21}(z)})/\tau_{21}(z)$, which is $\simeq 1$ until reionization begins; on the other, $x_{\text{coll}}(z)$ and $x_\alpha(z)$ are described by more complicated expressions, which require knowledge of the particle number density (for x_{coll}) or of the Lyα flux (for x_α). The latter, in particular, can be estimated as a function of the star formation rate density [161], as

$$J_\alpha(\boldsymbol{x}, z) = \frac{(1+z)^2}{4\pi} \int dR \dot{\rho}_* \epsilon_\alpha(\nu'), \quad \text{(B5)}$$

where $\epsilon_\alpha(\nu')$ indicates the spectral energy distribution in the Lyα to continuum regime.

Extensive review on the 21-cm signal can be found in Refs. [85–87].

Appendix C: Contour plots

We show in Figs. 12 and 13 the 1σ and 2σ confidence contours obtained from our analysis in Sec. IV. We include these triangle plots to highlight any potential degeneracy between cosmological and astrophysical parameters. To be concise, we only show the mIν model, since this is the case that requires 21-cm to explore new regions of parameter space beyond the capabilities of CMB experiments.

Note that τ is not included in the figures. Its uncertainty cannot be estimated from the 21-cm signal. In the case of cosmic dawn, we derive forecast constraints on τ as a function of the other parameters; see Eq. (32) and the related discussion.
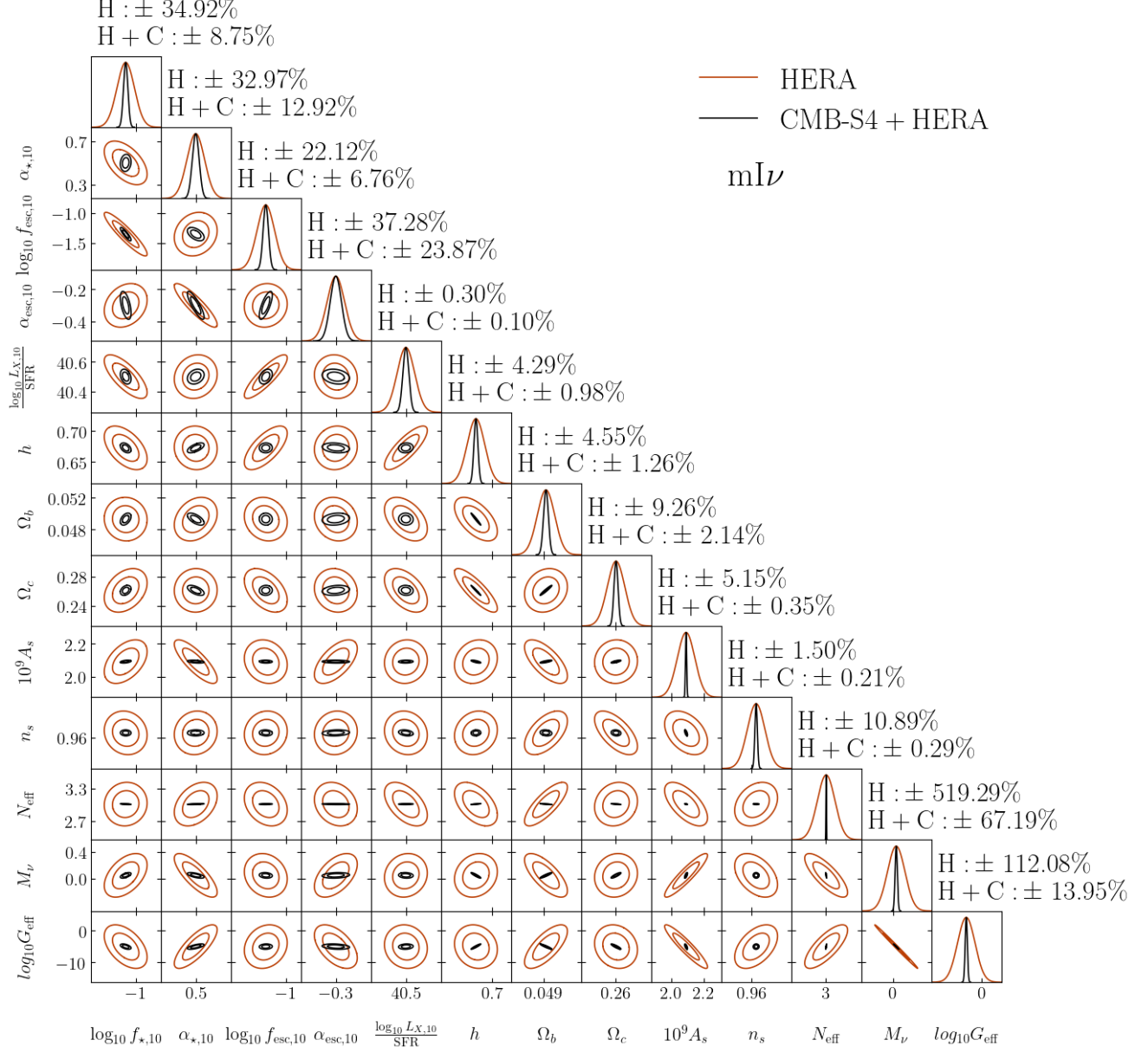
FIG. 12. Confidence ellipses and 2σ forecast uncertainties for all cosmological and astrophysical parameters in the HERA (H, red) and HERA+CMB-S4 (H+C, black) analysis, for the mIν model.
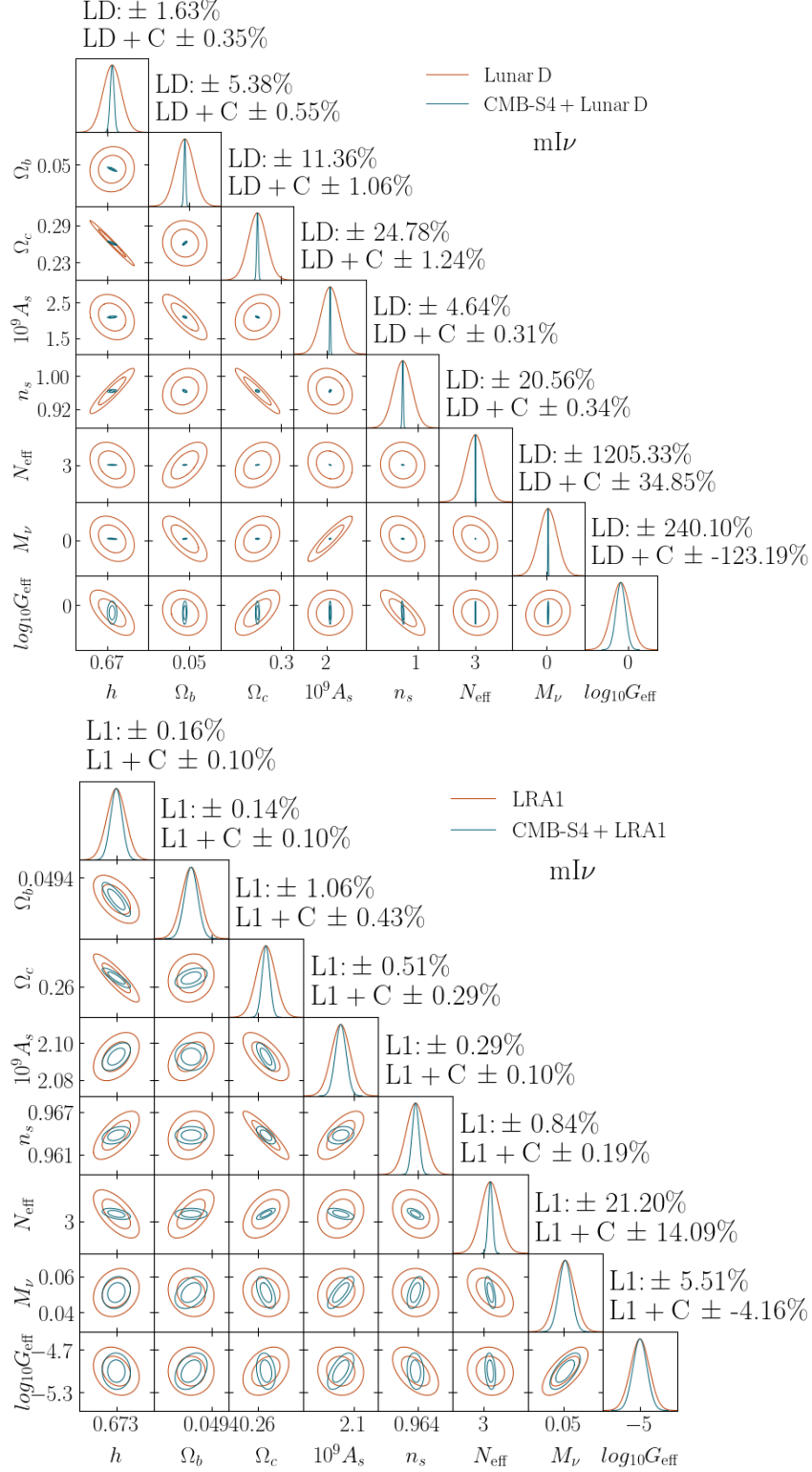
FIG. 13. Confidence ellipses and 2σ forecast uncertainties for the cosmological parameters in the mIν model, using Lunar D (top) and LRA1 (bottom), alone (red) or in combination with CMB-S4 (black).

[1] Y. Fukuda *et al.* (Super-Kamiokande), "Evidence for oscillation of atmospheric neutrinos," Phys. Rev. Lett. **81**, 1562–1567 (1998), arXiv:hep-ex/9807003.

[2] S. Fukuda *et al.* (Super-Kamiokande), "Constraints on neutrino oscillations using 1258 days of Super-Kamiokande solar neutrino data," Phys. Rev. Lett. **86**, 5656–5660 (2001), arXiv:hep-ex/0103033.

[3] S. Fukuda *et al.* (Super-Kamiokande), "Determination of solar neutrino oscillation parameters using 1496 days of Super-Kamiokande I data," Phys. Lett. B **539**, 179–187 (2002), arXiv:hep-ex/0205075.

[4] W. W. M. Allison *et al.* (Soudan 2), "Measurement of the L/E distributions of atmospheric neutrinos in Soudan 2 and their interpretation as neutrino oscillations," Phys. Rev. D **68**, 113004 (2003), arXiv:hep-ex/0307069.

[5] G. Drexlin, "Final neutrino oscillation results from LSND and KARMEN," Nucl. Phys. B Proc. Suppl. **118**, 146–153 (2003).

[6] T. Araki *et al.* (KamLAND), "Measurement of neutrino oscillation with KamLAND: Evidence of spectral distortion," Phys. Rev. Lett. **94**, 081801 (2005), arXiv:hep-ex/0406035.

[7] Y. Ashie *et al.* (Super-Kamiokande), "A Measurement of atmospheric neutrino oscillation parameters by SUPER-KAMIOKANDE I," Phys. Rev. D **71**, 112005 (2005), arXiv:hep-ex/0501064.

[8] M. D. Messier, "Review of neutrino oscllations experiments," eConf **C060409**, 018 (2006), arXiv:hep-ex/0606013.

[9] F. P. An *et al.* (Daya Bay), "Observation of electron-antineutrino disappearance at Daya Bay," Phys. Rev. Lett. **108**, 171803 (2012), arXiv:1203.1669 [hep-ex].

[10] Daniel J. Eisenstein and Wayne Hu, "Power spectra for cold dark matter and its variants," Astrophys. J. **511**, 5 (1997), arXiv:astro-ph/9710252.

[11] Jacob Brandbyge, Steen Hannestad, Troels Haugbølle, and Yvonne Y. Y. Wong, "Neutrinos in Non-linear Structure Formation - The Effect on Halo Properties," JCAP **09**, 014 (2010), arXiv:1004.4105 [astro-ph.CO].

[12] Federico Marulli, Carmelita Carbone, Matteo Viel, Lauro Moscardini, and Andrea Cimatti, "Effects of Massive Neutrinos on the Large-Scale Structure of the Universe," Mon. Not. Roy. Astron. Soc. **418**, 346 (2011), arXiv:1103.0278 [astro-ph.CO].

[13] Emanuele Castorina, Carmelita Carbone, Julien Bel, Emiliano Sefusatti, and Klaus Dolag, "DEMNUni: The clustering of large-scale structures in the presence of massive neutrinos," JCAP **07**, 043 (2015), arXiv:1505.07148 [astro-ph.CO].

[14] Eric Gawiser and Joseph Silk, "The Cosmic microwave background radiation," Phys. Rept. **333**, 245–267 (2000), arXiv:astro-ph/0002044.

[15] A. G. Doroshkevich, Y. B. Zeldovich, R. A. Sunyaev, and M. Khlopov, "Astrophysical implications of the neutrino rest mass. II. The density-perturbation spectrum and small-scale fluctuations in the microwave background," Sov. Astron. Lett. **6**, 252–256 (1980).

[16] N. Aghanim *et al.* (Planck), "Planck 2018 results. VI. Cosmological parameters," Astron. Astrophys. **641**, A6 (2020), [Erratum: Astron.Astrophys. 652, C4 (2021)], arXiv:1807.06209 [astro-ph.CO].

[17] A. G. Adame *et al.* (DESI), "DESI 2024 VI: Cosmological Constraints from the Measurements of Baryon Acoustic Oscillations," (2024), arXiv:2404.03002 [astro-ph.CO].

[18] Itamar J. Allali and Alessio Notari, "Neutrino mass bounds from DESI 2024 are relaxed by Planck PR4 and cosmological supernovae," JCAP **12**, 020 (2024), arXiv:2406.14554 [astro-ph.CO].

[19] M. Abdul Karim *et al.* (DESI), "DESI DR2 Results II: Measurements of Baryon Acoustic Oscillations and Cosmological Constraints," (2025), arXiv:2503.14738 [astro-ph.CO].

[20] W. Elbers *et al.* (DESI), "Constraints on Neutrino Physics from DESI DR2 BAO and DR1 Full Shape," (2025), arXiv:2503.14744 [astro-ph.CO].

[21] M. Aker *et al.* (KATRIN), "KATRIN: status and prospects for the neutrino mass and beyond," J. Phys. G **49**, 100501 (2022), arXiv:2203.08059 [nucl-ex].

[22] A. Ashtari Esfahani *et al.* (Project 8), "The Project 8 Neutrino Mass Experiment," in *Snowmass 2021* (2022) arXiv:2203.07349 [nucl-ex].

[23] Laura Herold and Marc Kamionkowski, "Revisiting the impact of neutrino mass hierarchies on neutrino mass constraints in light of recent DESI data," (2024), arXiv:2412.03546 [astro-ph.CO].

[24] Francis-Yan Cyr-Racine and Kris Sigurdson, "Limits on Neutrino-Neutrino Scattering in the Early Universe," Phys. Rev. D **90**, 123533 (2014), arXiv:1306.1536 [astro-ph.CO].

[25] Maria Archidiacono and Steen Hannestad, "Updated constraints on non-standard neutrino interactions from Planck," JCAP **07**, 046 (2014), arXiv:1311.3873 [astro-ph.CO].

[26] Francesco Forastieri, Massimiliano Lattanzi, Gianpiero Mangano, Alessandro Mirizzi, Paolo Natoli, and Ninetta Saviano, "Cosmic microwave background constraints on secret interactions among sterile neutrinos," JCAP **07**, 038 (2017), arXiv:1704.00626 [astro-ph.CO].

[27] Isabel M. Oldengott, Thomas Tram, Cornelius Rampf, and Yvonne Y. Y. Wong, "Interacting neutrinos in cosmology: exact description and constraints," JCAP **11**, 027 (2017), arXiv:1706.02123 [astro-ph.CO].

[28] Christina D. Kreisch, Francis-Yan Cyr-Racine, and Olivier Doré, "Neutrino puzzle: Anomalies, interactions, and cosmological tensions," Phys. Rev. D **101**, 123505 (2020), arXiv:1902.00534 [astro-ph.CO].

[29] Shouvik Roy Choudhury, Steen Hannestad, and Thomas Tram, "Updated constraints on massive neutrino self-interactions from cosmology in light of the H_0 tension," JCAP **03**, 084 (2021), arXiv:2012.07519 [astro-ph.CO].

[30] Subhajit Ghosh, Rishi Khatri, and Tuhin S. Roy, "Can dark neutrino interactions phase out the Hubble tension?" Phys. Rev. D **102**, 123544 (2020), arXiv:1908.09843 [hep-ph].

[31] Anirban Das and Subhajit Ghosh, "Flavor-specific interaction favors strong neutrino self-coupling in the early universe," JCAP **07**, 038 (2021), arXiv:2011.12315 [astro-ph.CO].

[32] Anirban Das and Subhajit Ghosh, "The magnificent

ACT of flavor-specific neutrino self-interaction," JCAP **09**, 042 (2023), arXiv:2303.08843 [astro-ph.CO].

[33] Lachlan Lancaster, Francis-Yan Cyr-Racine, Lloyd Knox, and Zhen Pan, "A tale of two modes: Neutrino free-streaming in the early universe," JCAP **07**, 033 (2017), arXiv:1704.06657 [astro-ph.CO].

[34] Brent Follin, Lloyd Knox, Marius Millea, and Zhen Pan, "First Detection of the Acoustic Oscillation Phase Shift Expected from the Cosmic Neutrino Background," Phys. Rev. Lett. **115**, 091301 (2015), arXiv:1503.07863 [astro-ph.CO].

[35] Daniel Baumann, Daniel Green, Joel Meyers, and Benjamin Wallisch, "Phases of New Physics in the CMB," JCAP **01**, 007 (2016), arXiv:1508.06342 [astro-ph.CO].

[36] Gabriele Montefalcone, Benjamin Wallisch, and Katherine Freese, "Free-Streaming Neutrinos and Their Phase Shift in Current and Future CMB Power Spectra," (2025), arXiv:2501.13788 [astro-ph.CO].

[37] Isabel M. Oldengott, Cornelius Rampf, and Yvonne Y. Y. Wong, "Boltzmann hierarchy for interacting neutrinos I: formalism," JCAP **04**, 016 (2015), arXiv:1409.1577 [astro-ph.CO].

[38] David Camarena, Francis-Yan Cyr-Racine, and John Houghteling, "Confronting self-interacting neutrinos with the full shape of the galaxy power spectrum," Phys. Rev. D **108**, 103535 (2023), arXiv:2309.03941 [astro-ph.CO].

[39] Adèle Poudou, Théo Simon, Thomas Montandon, Elsa M. Teixeira, and Vivian Poulin, "Self-interacting neutrinos in light of recent CMB and LSS data," (2025), arXiv:2503.10485 [astro-ph.CO].

[40] Adam He, Rui An, Mikhail M. Ivanov, and Vera Gluscevic, "Self-interacting neutrinos in light of large-scale structure data," Phys. Rev. D **109**, 103527 (2024), arXiv:2309.03956 [astro-ph.CO].

[41] Adam He, Mikhail M. Ivanov, Simeon Bird, Rui An, and Vera Gluscevic, "A Fresh Look at Neutrino Self-Interactions With the Lyman-α Forest: Constraints from EFT and PRIYA," (2025), arXiv:2503.15592 [astro-ph.CO].

[42] Antara Dey, Arnab Paul, and Supratik Pal, "Constraints on dark matter–neutrino interaction from 21-cm cosmology and forecasts on SKA1-Low," Mon. Not. Roy. Astron. Soc. **524**, 100–107 (2023), arXiv:2207.02451 [astro-ph.CO].

[43] Markus R. Mosbech, Celine Boehm, and Yvonne Y. Y. Wong, "Probing dark matter interactions with 21cm observations," JCAP **03**, 047 (2023), arXiv:2207.03107 [astro-ph.CO].

[44] Mansi Dhuria and Bishnu Gupta Teli, "Probing self-interacting ultrahigh-energy neutrinos with the cosmic 21-cm signal," Phys. Rev. D **110**, 123033 (2024), arXiv:2406.19279 [hep-ph].

[45] Adrian Liu, Jonathan R. Pritchard, Rupert Allison, Aaron R. Parsons, Uroš Seljak, and Blake D. Sherwin, "Eliminating the optical depth nuisance from the CMB with 21 cm cosmology," Phys. Rev. D **93**, 043013 (2016), arXiv:1509.08463 [astro-ph.CO].

[46] Gali Shmueli, Debanjan Sarkar, and Ely D. Kovetz, "Mitigating the optical depth degeneracy in the cosmological measurement of neutrino masses using 21-cm observations," Phys. Rev. D **108**, 083531 (2023), arXiv:2305.07056 [astro-ph.CO].

[47] David Camarena and Francis-Yan Cyr-Racine, "Strong constraints on a simple self-interacting neutrino cosmology," Phys. Rev. D **111**, 023504 (2025), arXiv:2403.05496 [astro-ph.CO].

[48] David R. DeBoer et al., "Hydrogen Epoch of Reionization Array (HERA)," Publ. Astron. Soc. Pac. **129**, 045001 (2017), arXiv:1606.07473 [astro-ph.IM].

[49] Robert Braun, Tyler Bourke, James A Green, Evan Keane, and Jeff Wagg, "Advancing Astrophysics with the Square Kilometre Array," PoS **AASKA14**, 174 (2015).

[50] Robert Braun, Anna Bonaldi, Tyler Bourke, Evan Keane, and Jeff Wagg, "Anticipated Performance of the Square Kilometre Array – Phase 1 (SKA1)," (2019), arXiv:1912.12699 [astro-ph.IM].

[51] Zara Abdurashidova et al. (HERA), "First Results from HERA Phase I: Upper Limits on the Epoch of Reionization 21 cm Power Spectrum," Astrophys. J. **925**, 221 (2022), arXiv:2108.02263 [astro-ph.CO].

[52] Zara Abdurashidova et al. (HERA), "HERA Phase I Limits on the Cosmic 21 cm Signal: Constraints on Astrophysics and Cosmology during the Epoch of Reionization," Astrophys. J. **924**, 51 (2022), arXiv:2108.07282 [astro-ph.CO].

[53] Hovav Lazare, Debanjan Sarkar, and Ely D. Kovetz, "HERA bound on x-ray luminosity when accounting for population III stars," Phys. Rev. D **109**, 043523 (2024), arXiv:2307.15577 [astro-ph.CO].

[54] Joseph Silk, "The limits of cosmology: role of the Moon," Phil. Trans. A. Math. Phys. Eng. Sci. **379**, 20190561 (2021), arXiv:2011.04671 [astro-ph.CO].

[55] Xuelei Chen et al., "Large-scale Array for Radio Astronomy on the Farside," Phil. Trans. Roy. Soc. Lond. A **382**, 20230094 (2024), arXiv:2403.16409 [astro-ph.IM].

[56] Parameswaran Ajith et al., "The Lunar Gravitational-wave Antenna: mission studies and science case," JCAP **01**, 108 (2025), arXiv:2404.09181 [gr-qc].

[57] Jack Burns et al., "A Lunar Farside Low Radio Frequency Array for Dark Ages 21-cm Cosmology," (2021), arXiv:2103.08623 [astro-ph.IM].

[58] Xuelei Chen, Jingye Yan, Li Deng, Fengquan Wu, Lin Wu, Yidong Xu, and Li Zhou, "Discovering the Sky at the Longest wavelengths with a lunar orbit array," Phil. Trans. Roy. Soc. Lond. A **379**, 20190566 (2020), arXiv:2007.15794 [astro-ph.IM].

[59] Benjamin R. B. Saliwanchik, Sven Herrmann, Ivan Kotov, Paul O'Connor, Maxim Potekhin, Anže Slosar, and Stuart Bale, "LuSEE-Night power requirements and power generation strategy," Proc. SPIE Int. Soc. Opt. Eng. **13102**, 131021G (2024), arXiv:2407.07173 [astro-ph.IM].

[60] Tianyang Liu, Jiajun Zhang, Yuan Shi, Junhua Gu, Quan Guo, Yidong Xu, Furen Deng, Fengquan Wu, Yanping Cong, and Xuelei Chen, "Forecast measurement of the 21 cm global spectrum from Lunar orbit with the Vari-Zeroth-Order Polynomial (VZOP) method," (2024), arXiv:2406.17000 [astro-ph.IM].

[61] Joseph Silk, "Cosmic black body radiation and galaxy formation," Astrophys. J. **151**, 459–471 (1968).

[62] Diego Blas, Julien Lesgourgues, and Thomas Tram, "The Cosmic Linear Anisotropy Solving System (CLASS) II: Approximation schemes," JCAP **07**, 034 (2011), arXiv:1104.2933 [astro-ph.CO].

[63] Jordan Flitter and Ely D. Kovetz, "New tool for 21-cm cosmology. II. Investigating the effect of early lin-

ear fluctuations," Phys. Rev. D **109**, 043513 (2024), arXiv:2309.03948 [astro-ph.CO].

[64] Jordan Flitter and Ely D. Kovetz, "New tool for 21-cm cosmology. I. Probing ΛCDM and beyond," Phys. Rev. D **109**, 043512 (2024), arXiv:2309.03942 [astro-ph.CO].

[65] Jordan Flitter, Sarah Libanore, and Ely D. Kovetz, "Does it matter? A more careful treatment of density fluctuations in 21-cm simulations," (2024), arXiv:2411.00089 [astro-ph.CO].

[66] Andrei Mesinger, Steven Furlanetto, and Renyue Cen, "21cmFAST: A Fast, Semi-Numerical Simulation of the High-Redshift 21-cm Signal," Mon. Not. Roy. Astron. Soc. **411**, 955 (2011), arXiv:1003.3878 [astro-ph.CO].

[67] Julien Lesgourgues and Sergio Pastor, "Massive neutrinos and cosmology," Phys. Rept. **429**, 307–379 (2006), arXiv:astro-ph/0603494.

[68] A. D. Dolgov, "Neutrinos in cosmology," Phys. Rept. **370**, 333–535 (2002), arXiv:hep-ph/0202122.

[69] Ziad Sakr, "A Short Review on the Latest Neutrinos Mass and Number Constraints from Cosmological Observables," Universe **8**, 284 (2022).

[70] V. F. Shvartsman, "Density of relict particles with zero rest mass in the universe," Pisma Zh. Eksp. Teor. Fiz. **9**, 315–317 (1969).

[71] G. Steigman, D. N. Schramm, and J. E. Gunn, "Cosmological Limits to the Number of Massive Leptons," Phys. Lett. B **66**, 202–204 (1977).

[72] S. Tremaine and J. E. Gunn, "Dynamical Role of Light Neutral Leptons in Cosmology," Phys. Rev. Lett. **42**, 407–410 (1979).

[73] Z. Chacko, Lawrence J. Hall, Takemichi Okui, and Steven J. Oliver, "CMB signals of neutrino mass generation," Phys. Rev. D **70**, 085008 (2004), arXiv:hep-ph/0312267.

[74] John F. Beacom, Nicole F. Bell, and Scott Dodelson, "Neutrinoless universe," Phys. Rev. Lett. **93**, 121302 (2004), arXiv:astro-ph/0404585.

[75] Nicole F. Bell, Elena Pierpaoli, and Kris Sigurdson, "Cosmological signatures of interacting neutrinos," Phys. Rev. D **73**, 063523 (2006), arXiv:astro-ph/0511410.

[76] Maximilian Berbig, Sudip Jana, and Andreas Trautner, "The Hubble tension and a renormalizable model of gauged neutrino self-interactions," Phys. Rev. D **102**, 115008 (2020), arXiv:2004.13039 [hep-ph].

[77] Hong-Jian He, Yin-Zhe Ma, and Jiaming Zheng, "Resolving Hubble Tension by Self-Interacting Neutrinos with Dirac Seesaw," JCAP **11**, 003 (2020), arXiv:2003.12057 [hep-ph].

[78] Florian Beutler, Chris Blake, Matthew Colless, D. Heath Jones, Lister Staveley-Smith, Lachlan Campbell, Quentin Parker, Will Saunders, and Fred Watson, "The 6dF Galaxy Survey: Baryon Acoustic Oscillations and the Local Hubble Constant," Mon. Not. Roy. Astron. Soc. **416**, 3017–3032 (2011), arXiv:1106.3366 [astro-ph.CO].

[79] Ashley J. Ross, Lado Samushia, Cullan Howlett, Will J. Percival, Angela Burden, and Marc Manera, "The clustering of the SDSS DR7 main Galaxy sample – I. A 4 per cent distance measure at $z = 0.15$," Mon. Not. Roy. Astron. Soc. **449**, 835–847 (2015), arXiv:1409.3242 [astro-ph.CO].

[80] Shadab Alam *et al.* (BOSS), "The clustering of galaxies in the completed SDSS-III Baryon Oscillation Spectro-

scopic Survey: cosmological analysis of the DR12 galaxy sample," Mon. Not. Roy. Astron. Soc. **470**, 2617–2652 (2017), arXiv:1607.03155 [astro-ph.CO].

[81] Sergei Bashinsky and Uros Seljak, "Neutrino perturbations in CMB anisotropy and matter clustering," Phys. Rev. D **69**, 083002 (2004), arXiv:astro-ph/0310198.

[82] José Luis Bernal, Tristan L. Smith, Kimberly K. Boddy, and Marc Kamionkowski, "Robustness of baryon acoustic oscillation constraints for early-Universe modifications of ΛCDM cosmology," Phys. Rev. D **102**, 123515 (2020), arXiv:2004.07263 [astro-ph.CO].

[83] Chung-Pei Ma and Edmund Bertschinger, "Cosmological perturbation theory in the synchronous versus conformal Newtonian gauge," (1994), arXiv:astro-ph/9401007.

[84] Alvise Raccanelli, Licia Verde, and Francisco Villaescusa-Navarro, "Biases from neutrino bias: to worry or not to worry?" Mon. Not. Roy. Astron. Soc. **483**, 734–743 (2019), arXiv:1704.07837 [astro-ph.CO].

[85] Rennan Barkana and Abraham Loeb, "In the beginning: The First sources of light and the reionization of the Universe," Phys. Rept. **349**, 125–238 (2001), arXiv:astro-ph/0010468.

[86] Steven Furlanetto, S. Peng Oh, and Frank Briggs, "Cosmology at Low Frequencies: The 21 cm Transition and the High-Redshift Universe," Phys. Rept. **433**, 181–301 (2006), arXiv:astro-ph/0608032.

[87] Jonathan R. Pritchard and Abraham Loeb, "21-cm cosmology," Rept. Prog. Phys. **75**, 086901 (2012), arXiv:1109.6012 [astro-ph.CO].

[88] S. A. Wouthuysen, "On the excitation mechanism of the 21-cm (radio-frequency) interstellar hydrogen emission line." Astronomical Journal **57**, 31–32 (1952).

[89] George B. Field, "Excitation of the Hydrogen 21-CM Line," Proceedings of the IRE **46**, 240–250 (1958).

[90] S. Peng Oh, "Reionization by hard photons: I. x-rays from the first star clusters," Astrophys. J. **553**, 499 (2001), arXiv:astro-ph/0005262.

[91] Massimo Ricotti and Jeremiah P. Ostriker, "X-ray preionization powered by accretion on the first black holes. 1: A Model for the WMAP polarisation measurement," Mon. Not. Roy. Astron. Soc. **352**, 547 (2004), arXiv:astro-ph/0311003.

[92] Jonathan R. Pritchard and Steven R. Furlanetto, "21 cm fluctuations from inhomogeneous X-ray heating before reionization," Mon. Not. Roy. Astron. Soc. **376**, 1680–1694 (2007), arXiv:astro-ph/0607234.

[93] Raghunath Ghara *et al.*, "Probing the intergalactic medium during the Epoch of Reionization using 21 cm signal power spectra," Astron. Astrophys. **687**, A252 (2024), arXiv:2404.11686 [astro-ph.CO].

[94] Jaehong Park, Andrei Mesinger, Bradley Greig, and Nicolas Gillet, "Inferring the astrophysics of reionization and cosmic dawn from galaxy luminosity functions and the 21-cm signal," Mon. Not. Roy. Astron. Soc. **484**, 933–949 (2019), arXiv:1809.08995 [astro-ph.GA].

[95] Julian B. Muñoz, Yuxiang Qin, Andrei Mesinger, Steven G. Murray, Bradley Greig, and Charlotte Mason, "The impact of the first galaxies on cosmic dawn and reionization," Mon. Not. Roy. Astron. Soc. **511**, 3657–3681 (2022), arXiv:2110.13919 [astro-ph.CO].

[96] William H. Press and Paul Schechter, "Formation of galaxies and clusters of galaxies by selfsimilar gravitational condensation," Astrophys. J. **187**, 425–438

(1974).

[97] J. R. Bond, S. Cole, G. Efstathiou, and Nick Kaiser, "Excursion set mass functions for hierarchical Gaussian fluctuations," Astrophys. J. **379**, 440 (1991).

[98] J. L. Friedman and B. F. Schutz, "Lagrangian perturbation theory of nonrelativistic fluids." Astrophys. J. **221**, 937–957 (1978).

[99] T. Buchert, "A class of solutions in Newtonian cosmology and the pancake theory," Astron. Astrophys. **223**, 9–24 (1989).

[100] Rennan Barkana and Abraham Loeb, "Unusually large fluctuations in the statistics of galaxy formation at high redshift," Astrophys. J. **609**, 474–481 (2004), arXiv:astro-ph/0310338.

[101] Rennan Barkana and Abraham Loeb, "The Difference PDF of 21-cm Fluctuations: A Powerful Statistical Tool for Probing Cosmic Reionization," Mon. Not. Roy. Astron. Soc. **384**, 1069 (2008), arXiv:0705.3246 [astro-ph].

[102] Ravi K. Sheth and Giuseppe Tormen, "Large scale bias and the peak background split," Mon. Not. Roy. Astron. Soc. **308**, 119 (1999), arXiv:astro-ph/9901122.

[103] Ravi K. Sheth, H. J. Mo, and Giuseppe Tormen, "Ellipsoidal collapse and an improved model for the number and spatial distribution of dark matter haloes," Mon. Not. Roy. Astron. Soc. **323**, 1 (2001), arXiv:astro-ph/9907024.

[104] Ravi K. Sheth and Giuseppe Tormen, "An Excursion Set Model of Hierarchical Clustering : Ellipsoidal Collapse and the Moving Barrier," Mon. Not. Roy. Astron. Soc. **329**, 61 (2002), arXiv:astro-ph/0105113.

[105] Ivan Nikolić, Andrei Mesinger, James E. Davies, and David Prelogović, "The importance of stochasticity in determining galaxy emissivities and UV LFs during cosmic dawn and reionization," (2024), arXiv:2406.15237 [astro-ph.CO].

[106] James Davies, Andrei Mesinger, and et al., "In preparation,".

[107] Max Tegmark, Joseph Silk, Martin J. Rees, Alain Blanchard, Tom Abel, and Francesco Palla, "How small were the first cosmological objects?" Astrophys. J. **474**, 1–12 (1997), arXiv:astro-ph/9603007.

[108] Tom Abel, Greg L. Bryan, and Michael L. Norman, "The formation of the first star in the Universe," Science **295**, 93 (2002), arXiv:astro-ph/0112088.

[109] Volker Bromm and Richard B. Larson, "The First stars," Ann. Rev. Astron. Astrophys. **42**, 79–118 (2004), arXiv:astro-ph/0311019.

[110] Michele Trenti, "Population III Star Formation During and After the Reionization Epoch," AIP Conf. Proc. **1294**, 134–137 (2010), arXiv:1006.4434 [astro-ph.CO].

[111] Sarah Libanore, Jordan Flitter, Ely D. Kovetz, Zhaozhou Li, and Avishai Dekel, "Effects of feedback-free starburst galaxies on the 21-cm signal and reionization history," Mon. Not. Roy. Astron. Soc. **532**, 149–163 (2024), arXiv:2310.03021 [astro-ph.CO].

[112] Julian B. Muñoz, "An Effective Model for the Cosmic-Dawn 21-cm Signal," (2023), 10.1093/mnras/stad1512, arXiv:2302.08506 [astro-ph.CO].

[113] Hector Afonso G. Cruz, Tal Adi, Jordan Flitter, Marc Kamionkowski, and Ely D. Kovetz, "21-cm fluctuations from primordial magnetic fields," Phys. Rev. D **109**, 023518 (2024), arXiv:2308.04483 [astro-ph.CO].

[114] Lam Hui and Nickolay Y. Gnedin, "Equation of state of the photoionized intergalactic medium," Mon. Not. Roy. Astron. Soc. **292**, 27 (1997), arXiv:astro-ph/9612232.

[115] Takashi Okamoto, Liang Gao, and Tom Theuns, "Mass-loss of galaxies due to a UV-background," Mon. Not. Roy. Astron. Soc. **390**, 920 (2008), arXiv:0806.0378 [astro-ph].

[116] Pierre Ocvirk et al., "Cosmic Dawn II (CoDa II): a new radiation-hydrodynamics simulation of the self-consistent coupling of galaxy formation and reionization," Mon. Not. Roy. Astron. Soc. **496**, 4087–4107 (2020), arXiv:1811.11192 [astro-ph.GA].

[117] Harley Katz et al., "How to Quench a Dwarf Galaxy: The Impact of Inhomogeneous Reionization on Dwarf Galaxies and Cosmic Filaments," Mon. Not. Roy. Astron. Soc. **494**, 2200–2220 (2020), arXiv:1905.11414 [astro-ph.GA].

[118] Yuxiang Qin, Andrei Mesinger, Jaehong Park, Bradley Greig, and Julian B. Muñoz, "A tale of two sites – I. Inferring the properties of minihalo-hosted galaxies from current observations," Mon. Not. Roy. Astron. Soc. **495**, 123–140 (2020), arXiv:2003.04442 [astro-ph.CO].

[119] Mihir Kulkarni, Eli Visbal, and Greg L. Bryan, "The Critical Dark Matter Halo Mass for Population III Star Formation: Dependence on Lyman–Werner Radiation, Baryon-dark Matter Streaming Velocity, and Redshift," Astrophys. J. **917**, 40 (2021), arXiv:2010.04169 [astro-ph.GA].

[120] Dmitriy Tseliakhovich and Christopher Hirata, "Relative velocity of dark matter and baryonic fluids and the formation of the first structures," Phys. Rev. D **82**, 083520 (2010), arXiv:1005.2416 [astro-ph.CO].

[121] Smadar Naoz, Naoki Yoshida, and Nickolay Y. Gnedin, "Simulations of Early Baryonic Structure Formation with Stream Velocity: I. Halo Abundance," Astrophys. J. **747**, 128 (2012), arXiv:1108.5176 [astro-ph.CO].

[122] Athena Stacy, Volker Bromm, and Abraham Loeb, "Effect of Streaming Motion of Baryons Relative to Dark Matter on the Formation of the First Stars," Astrophys. J. Lett. **730**, L1 (2011), arXiv:1011.4512 [astro-ph.CO].

[123] Jo Bovy and Cora Dvorkin, "Low-mass suppression of the satellite luminosity function due to the supersonic baryon–cold-dark-matter relative velocity," Astrophys. J. **768**, 70 (2013), arXiv:1205.2083 [astro-ph.CO].

[124] Fabian Schmidt, "Effect of relative velocity and density perturbations between baryons and dark matter on the clustering of galaxies," Phys. Rev. D **94**, 063508 (2016), arXiv:1602.09059 [astro-ph.CO].

[125] Yacine Ali-Haïmoud, P. Daniel Meerburg, and Sihan Yuan, "New light on 21 cm intensity fluctuations from the dark ages," Phys. Rev. D **89**, 083506 (2014), arXiv:1312.4948 [astro-ph.CO].

[126] Julian B. Muñoz, "Standard ruler at cosmic dawn," Physical Review Letters **123** (2019), 10.1103/physrevlett.123.131301.

[127] Benedetta Ciardi, E. Scannapieco, F. Stoehr, A. Ferrara, I. T. Iliev, and P. R. Shapiro, "The effect of minihaloes on cosmic reionization," Mon. Not. Roy. Astron. Soc. **366**, 689–696 (2006), arXiv:astro-ph/0511623.

[128] Taysun Kimm, Harley Katz, Martin Haehnelt, Joakim Rosdahl, Julien Devriendt, and Adrianne Slyz, "Feedback-regulated star formation and escape of LyC photons from mini-haloes during reionization," Mon. Not. Roy. Astron. Soc. **466**, 4826–4846 (2017), arXiv:1608.04762 [astro-ph.GA].

[129] Jonathan C. Pober, Aaron R. Parsons, David R. De-

Boer, Patrick McDonald, Matthew McQuinn, James E. Aguirre, Zaki Ali, Richard F. Bradley, Tzu-Ching Chang, and Miguel F. Morales, "The Baryon Acoustic Oscillation Broadband and Broad-beam Array: Design Overview and Sensitivity Forecasts," Astron. J. **145**, 65 (2013), arXiv:1210.2413 [astro-ph.CO].

[130] Jonathan C. Pober *et al.*, "What Next-Generation 21 cm Power Spectrum Measurements Can Teach Us About the Epoch of Reionization," Astrophys. J. **782**, 66 (2014), arXiv:1310.7031 [astro-ph.CO].

[131] Steven G. Murray, Jonathan Pober, and Matthew Kolopanis, "21cmSense v2: A modular, open-source 21cm sensitivity calculator," J. Open Source Softw. **9**, 6501 (2024), arXiv:2406.02415 [astro-ph.CO].

[132] Aaron R. Parsons, Jonathan C. Pober, James E. Aguirre, Christopher L. Carilli, Daniel C. Jacobs, and David F. Moore, "A Per-Baseline, Delay-Spectrum Technique for Accessing the 21cm Cosmic Reionization Signature," Astrophys. J. **756**, 165 (2012), arXiv:1204.4749 [astro-ph.IM].

[133] Garrelt Mellema *et al.*, "Reionization and the Cosmic Dawn with the Square Kilometre Array," Exper. Astron. **36**, 235–318 (2013), arXiv:1210.0197 [astro-ph.CO].

[134] Rajesh Mondal, Somnath Bharadwaj, and Suman Majumdar, "Statistics of the epoch of reionization 21-cm signal – I. Power spectrum error-covariance," Mon. Not. Roy. Astron. Soc. **456**, 1936–1947 (2016), arXiv:1508.00896 [astro-ph.CO].

[135] Rajesh Mondal and Rennan Barkana, "Prospects for precision cosmology with the 21 cm signal from the dark ages," Nature Astron. **7**, 1025–1030 (2023), arXiv:2305.08593 [astro-ph.CO].

[136] Adam Lidz, Oliver Zahn, Matthew McQuinn, Matias Zaldarriaga, and Lars Hernquist, "Detecting the Rise and Fall of 21 cm Fluctuations with the Murchison Widefield Array," Astrophys. J. **680**, 962–974 (2008), arXiv:0711.4373 [astro-ph].

[137] Rajesh Mondal, Somnath Bharadwaj, and Suman Majumdar, "Statistics of the epoch of reionization (EoR) 21-cm signal – II. The evolution of the power-spectrum error-covariance," Mon. Not. Roy. Astron. Soc. **464**, 2992–3004 (2017), arXiv:1606.03874 [astro-ph.CO].

[138] Matthew McQuinn, Oliver Zahn, Matias Zaldarriaga, Lars Hernquist, and Steven R. Furlanetto, "Cosmological parameter estimation using 21 cm radiation from the epoch of reionization," Astrophys. J. **653**, 815–830 (2006), arXiv:astro-ph/0512263.

[139] José Luis Bernal, Alvise Raccanelli, Licia Verde, and Joseph Silk, "Signatures of primordial black holes as seeds of supermassive black holes," JCAP **05**, 017 (2018), [Erratum: JCAP 01, E01 (2020)], arXiv:1712.01311 [astro-ph.CO].

[140] Eleonora Vanzan, Alvise Raccanelli, and Nicola Bartolo, "Dark ages, a window on the dark sector. Hunting for ultra-light axions," JCAP **03**, 001 (2024), arXiv:2306.09252 [astro-ph.CO].

[141] Jessie de Kruijf, Eleonora Vanzan, Kimberly K. Boddy, Alvise Raccanelli, and Nicola Bartolo, "Searching for blue in the dark," (2024), arXiv:2408.04991 [astro-ph.CO].

[142] Elena Vanetti, Eleonora Vanzan, Nicola Bellomo, and Alvise Raccanelli, "Testing the growth of cosmic structures during the Dark Ages," (2025), arXiv:2502.08562 [astro-ph.CO].

[143] Matias Zaldarriaga, Steven R. Furlanetto, and Lars Hernquist, "21 Centimeter fluctuations from cosmic gas at high redshifts," Astrophys. J. **608**, 622–635 (2004), arXiv:astro-ph/0311514.

[144] Srinivasan Raghunathan and Yuuki Omori, "A cross-internal linear combination approach to probe the secondary cmb anisotropies: Kinematic sunyaev-zel'dovich effect and cmb lensing," (2023), arXiv:2304.09166 [astro-ph.CO].

[145] Daniel Green, Joel Meyers, and Alexander van Engelen, "CMB Delensing Beyond the B Modes," JCAP **12**, 005 (2017), arXiv:1609.08143 [astro-ph.CO].

[146] Selim C. Hotinli, Joel Meyers, Cynthia Trendafilova, Daniel Green, and Alexander van Engelen, "The benefits of CMB delensing," JCAP **04**, 020 (2022), arXiv:2111.15036 [astro-ph.CO].

[147] C. L. Reichardt *et al.* (SPT), "An Improved Measurement of the Secondary Cosmic Microwave Background Anisotropies from the SPT-SZ + SPTpol Surveys," Astrophys. J. **908**, 199 (2021), arXiv:2002.06197 [astro-ph.CO].

[148] Kevork Abazajian *et al.* (CMB-S4), "CMB-S4: Forecasting Constraints on Primordial Gravitational Waves," Astrophys. J. **926**, 54 (2022), arXiv:2008.12619 [astro-ph.CO].

[149] Licia Verde, "Statistical methods in cosmology," Lect. Notes Phys. **800**, 147–177 (2010), arXiv:0911.3105 [astro-ph.CO].

[150] Kevork Abazajian *et al.*, "CMB-S4 Science Case, Reference Design, and Project Plan," (2019), arXiv:1907.04473 [astro-ph.IM].

[151] Simone Aiola *et al.* (ACT), "The Atacama Cosmology Telescope: DR4 Maps and Cosmological Parameters," JCAP **12**, 047 (2020), arXiv:2007.07288 [astro-ph.CO].

[152] Andrei Mesinger, Bradley Greig, and Emanuele Sobacchi, "The Evolution Of 21 cm Structure (EOS): public, large-scale simulations of Cosmic Dawn and reionization," Mon. Not. Roy. Astron. Soc. **459**, 2342–2353 (2016), arXiv:1602.07711 [astro-ph.CO].

[153] Aviad Cohen, Anastasia Fialkov, Rennan Barkana, and Matan Lotem, "Charting the Parameter Space of the Global 21-cm Signal," Mon. Not. Roy. Astron. Soc. **472**, 1915–1931 (2017), arXiv:1609.02312 [astro-ph.CO].

[154] George B. Field, "The Spin Temperature of Intergalactic Neutral Hydrogen." Astrophysical Journal **129**, 536 (1959).

[155] P. J. E. Peebles, "Recombination of the Primeval Plasma," Astrophys. J. **153**, 1 (1968).

[156] Chung-Pei Ma and Edmund Bertschinger, "Cosmological perturbation theory in the synchronous and conformal Newtonian gauges," Astrophys. J. **455**, 7–25 (1995), arXiv:astro-ph/9506072.

[157] Sara Seager, Dimitar D. Sasselov, and Douglas Scott, "A new calculation of the recombination epoch," Astrophys. J. Lett. **523**, L1–L5 (1999), arXiv:astro-ph/9909275.

[158] Sara Seager, Dimitar D. Sasselov, and Douglas Scott, "How exactly did the universe become neutral?" Astrophys. J. Suppl. **128**, 407–430 (2000), arXiv:astro-ph/9912182.

[159] Smadar Naoz and Rennan Barkana, "Growth of linear perturbations before the era of the first galaxies," Mon. Not. Roy. Astron. Soc. **362**, 1047–1053 (2005), arXiv:astro-ph/0503196.

[160] Christopher M. Hirata, "Wouthuysen-Field coupling strength and application to high-redshift 21 cm radiation," Mon. Not. Roy. Astron. Soc. **367**, 259–274 (2006), arXiv:astro-ph/0507102.

[161] Rennan Barkana and Abraham Loeb, "Detecting the earliest galaxies through two new sources of 21cm fluctuations," Astrophys. J. **626**, 1–11 (2005), arXiv:astro-ph/0410129.